Department of Physics and Astronomy
University of Heidelberg

Bachelor Thesis in Physics
submitted by

Christian Heppe

born in Heidelberg, Germany

2020

Short-wavelength radiation generation in ultra-relativistic laser-plasma interaction

This Bachelor Thesis has been carried out by Christian Heppe at the
Max Planck Institute for Nuclear Physics in Heidelberg
under the supervision of
Hon. Prof. Dr. Christoph Keitel and Dr. Naveen Kumar

Abstract

The generation of collimated high-energy high brilliance γ-rays by a high-intensity laser pulse impacting a structured plasma target in the ultra-relativistic regime, is investigated with several 2D PIC-simulations using results of recent research. Comparing sweeps of incident power for two fixed focused intensities of normalised laser amplitudes $a_0 = 190$ and $a_0 = 350$, for a 40 fs laser pulse revealed that a maximum brilliance of $1.9 \times 10^{19}\mathrm{s}^{-1}\mathrm{mm}^{-2}\mathrm{mrad}^{-2}(0.1\%BW)^{-1}$ for photon energies exceeding 100 MeV can be achieved at energy conversion efficiencies of up to 2.3%, generating copious amounts of multi-MeV photons driven by strong multi-MT quasi static magnetic plasma fields. In prospect of the construction of new laser facilities, which are expected to operate in radiation dominated regimes, the generation of such all-optical γ-rays offers opportunities for a broad spectrum of applications in many fields of research.

Zusammenfassung

Die Erzeugung kolimierter, hochenergetischer und brillianter γ-Strahlen durch den Beschuss strukturierter Plasmaziele mittels intensiver Laser Pulse im ultra-relativistischen Regime, wurde mit Hilfe von 2D PIC-Simulationen, aufbauend auf neuesten Forschungsergebnissen, untersucht. Der Vergleich von Leistungsscans zweier 40 fs Laser Pulse mit festen fokusierten Intensitäten für normalisierte Amplituden von $a_0 = 190$ und $a_0 = 350$ zeigte, dass eine maximale Brillianz von $1.9 \times 10^{19} \mathrm{s}^{-1}\mathrm{mm}^{-2}\mathrm{mrad}^{-2}(0.1\%BW)^{-1}$ für Photon-Energien von mehr als 100 MeV, mit einer Energie-Umwandlungs-Effizienz von bis zu 2.3% bei der Erzeugung einer Großzahl von multi-MeV Photonen durch MT starke quasistatische Plasma-Magnetfelder möglich ist. Mit Aussicht auf die Fertigstellung neuester Laser Einrichtungen, welche diese Reaktionsregime eröffnen sollen, bieten solche ausschließlich optischen γ-Strahlungsquellen Möglichkeiten für breite Anwendungsgebiete in vielen Forschungsfeldern.

Contents

1 Introduction

The current increase in technically achievable laser power and the resulting ultra-high intensities have opened up new possibilities for fundamental research as well as laboratory astrophysics and several other fields [2]. With the most powerful laser *Apollon* currently under construction in France, meant to achieve 10 PW pulses for a duration of 15 fs with peak intensities exceeding $2 \times 10^{22}\,\mathrm{Wcm}^{-2}$ [17] in the next years, new and unprecedented research possibilities are close to becoming experimental reality.
Achieving intensities approaching $10^{23}\,\mathrm{Wcm}^{-2}$ opens up the regime of laser-matter interactions in which radiation reaction significantly impacts the particle dynamics [5, 9, 14, 15]. In these extreme laser interactions the electron dynamics become ultra-relativistic ($|v_e| \approx c$) and quantum electrodynamic (QED) processes strongly impact the electron motion and energy distribution. In particular the generation of high-energy γ-photons by laser-matter interactions is of interest, as it offers the possibility to generate copious amounts of multi-MeV γ-photons in all optical setups. These multi-MeV γ-photon sources have numerous applications from fundamental research of radiation-reaction, generation of electron-positron (e^-e^+) pairs over photospectroscopy, radiotherapy and radiosurgery[2, 22].

Recent research showed, that special target geometries can enhance the multi-MeV γ-photon generation and provide better collimation of the resulting beam under high-intensity laser pulses [9, 10, 22]. Especially the geometry of a channel (conical or cylindrical) seems to create strong quasi-static magnetic fields enhancing multi-MeV γ-photons in a highly collimated high-brilliance beam [28]. For a given geometry and fixed laser intensity I_L the multi-MeV γ-photon generation increases with the incident laser power P_L [9]. Calculations modeling dynamic filamentation instabilities suggest that the MeV-photon emission saturates at a critical incident laser-power $P_{L,crit}$. To quantify and validate these findings several 2D particle-in-cell (PIC) simulations where done with the open-source code SMILEI [4]. In addition we examine the power conversion efficiency into high-energy photons and the collimation of the resulting beam.

2 Formalism

Laser-plasma reactions can be characterized by the used focused intensity of the laser. With rising intensities one leaves the classical regime and enters the regime of relativistic optics or laser-matter/laser-plasma interactions at focused intensities $\sim 10^{20}\,\mathrm{W/cm}^2$ (Fig. 1), where the dynamics of electrons become strongly relativistic. With these high intensities every laser-matter interaction is in good resemblance a laser-plasma interaction, since a solid target will be fully ionized before the peak of the laser-pulses intensity even reaches the target [9]. At further increasing levels of intensities exceeding $10^{23}\,\mathrm{W/cm}^2$, as are being offered by facilities under current construction [2, 17], laser-plasma interactions enter the radiation-dominated QED regime. Ultra-relativistic electrons absorb energy directly from present electromagnetic (EM) fields and emit high-energy photons [6, 9].

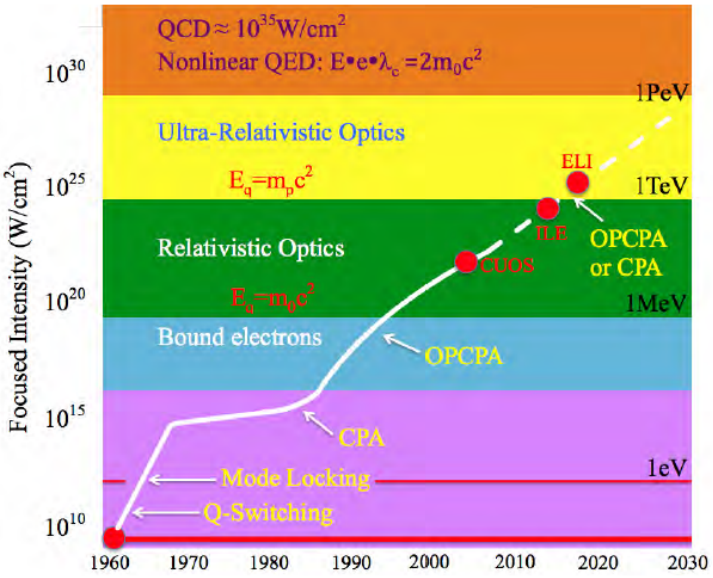

Figure 1: Schematic visualization of laser intensities over the years and corresponding interaction regimes. ILE/Apollon lasers as well as ELI are already plotted. ELI will be an installation of 10 ILE/Apollon-type beams [2].

Since the energies of interest for these emitted photons ($\gtrsim 10\,\mathrm{MeV}$) are of the same order as the electrons kinetic energy QED effects become important [5, 6, 14, 15]. In these high-energy regimes key characteristics of laser-plasma interactions are relativistic transparency experienced by the laser pulse [9, 13, 22], direct laser acceleration [22] and synchrotron photon emission [22] as well as non-linear Compton-scattering [28]. In addition to these effects the laser experiences strong non-linear filamentation instabilities resulting in the generation of emerging quasi-static magnetic fields [13, 20].

In this section the general formalism for the laser-plasma interactions and the appertaining radiation-reactions, laser-dynamics and generally occuring QED effects is set and qualitatively explained by taking a semi-classical approach.

2.1 Classical interaction and motion of laser pulses with matter

In order to understand the generation of high-energy multi-MeV γ-photons within laser-plasma reactions it is necessary to understand how the plasma reacts when being radiated by ultra-strong laser pulses. The lasers of interest have focused intensities of the order of $10^{22}\,\mathrm{W/cm^2}$ in pulses shorter then 10 fs with energy-fluctuations of $\frac{\Delta E}{E} \approx 1\%$ [2, 17, 28]. For computational ease, all of the interacting matter is assumed to be fully ionized and therefor already in it's plasma state. In reality this would happen instantaneously due to the immense laser intensity even before the pulse reaches it's maximum [9, 18]. This means that the former gaseous material has dissolved into two species of particles: The semi-freely moving electrons (e^-) and the ions to which the electrons were bound before. The degree of ionization

is given as:

$$\alpha = \frac{n_i}{n_i + n_n} \tag{2.1}$$

Where n_i is the number density of ions and n_n the number of neutral atoms. Since the plasma in question is fully ionized it is a good approximation to say $n_n \approx 0$ and therefor $\alpha \to 1$. Depending on which material is used one can create multiple times positively charged high-Z ions. The most commonly used targets in laboratories are out of Hydrogen (^1H) plasma, which consists of an electron and a proton ($e^- p$) for each initial neutral ^1H atom.

$$^1H \to e^- + p.$$

This means that initially the total number of electrons N_e is equal to the total number of ions N_i, which in this case are protons. Since all of the present particles have a charge of $\pm e$ with e being the elementary electronic charge, they are responsive to any present electromagnetic field and the equation of motion is given by the *Lorentz Equation*

$$\vec{F} = m_e \frac{d\vec{v}}{dt} = \pm e(\vec{E} + \vec{v} \times \vec{B}) \tag{2.2}$$

where m_e is the electron-mass m_e with negative elementary charge $-e$ [8, 11].
In the non relativistic case the impact of present magnetic fields on the moving particle are negligibly small so that the equation reduces to

$$\vec{F} = m_e \frac{d\vec{v}}{dt} = \pm e\vec{E}. \tag{2.3}$$

For a planar wave of light one can describe it's electric field component $\vec{E}$ at a point in space $\vec{r}$ and time t as

$$\vec{E}(\vec{r}, t) = E_0 cos(\omega t - \vec{k}\vec{r}), \tag{2.4}$$

with $\omega = 2\pi c/\lambda = ck$ the lasers angular frequency. The electric field $\vec{E}(\vec{r}, t)$ causes a charged particle to move along it's polarization as the laser pulse moves along the propagation axis $\hat{k}$, with

$$\hat{k} \equiv \frac{\vec{k}}{|\vec{k}|}.$$

Putting this oscillatory velocity given by Eq.Eq. (2.3) in Eq.Eq. (2.2), one can derive the so called *ponderomotive Force* that the laser's electric field exerts on the electrons of the plasma. The speed of this quivering movement is given by solving the equation of movement Eq. (2.3) for the given electric field Eq. (2.4) by integrating over time:

$$\vec{v_q} = \frac{\pm e E_0}{m_e} \int \text{dt } cos(\omega t - \vec{k}\vec{r}) \tag{2.5}$$

Yielding the following expression for the quiver velocity v_q

$$v_q = \frac{\pm eE_0}{m_e \omega}. \tag{2.6}$$

The angular frequency of the particles oscillation is given by ω following the pulses propagation $\vec{k}$. The energy U_p stored in this motion is given by $U_p = \langle \frac{1}{2} m_i v_q^2 \rangle_{cycle} = \frac{1}{2} \epsilon_{kin,max}$[11]

$$U_p = \frac{e^2 E_0^2}{4 m_i \omega^2} \tag{2.7}$$

A cycle in this case describes an electron following the laser pulse's electric field $\vec{E}(\vec{r}, t)$ for a whole period $T = 2\pi/\omega$. U_p defines the *Ponderomotive Potential* of the laser. For electrons this reads in practical units as

$$U_p = 9.33 \times 10^{-14} (\lambda[\mu\text{m}])^2 \; I_L \; [\text{W/cm}^2]\text{eV}. \tag{2.8}$$

Thus an exemplary pulse with $\lambda = 1\,\mu\text{m}$ and focused intensity of $I_L = 1 \times 10^{22}\,\text{W/cm}^2$ has a ponderomotive potential of $U_p = 933\,\text{MeV} \approx 1\,\text{GeV}$. [11]
Due to the conservative nature of the *ponderomotive force* we can now define it as the negative gradient of U_p:

$$F_p \equiv -\nabla U_p \tag{2.9}$$

But the previous calculation does not consider that the laser's wavefront is not perfectly planar. In realistic situations, the laser has a radial intensity profile, which is in good approximation resembled by a Gaussian distribution with it's peak intensity along the laser propagation axis $\hat{k}$. This present field gradient leads to an additional radial acceleration of the quivering particles towards lower intensity regions [8, 11].

$$F_p(\vec{r}, t) = -\frac{e^2}{4 m_e \omega^2} \nabla E_0^2(\vec{r}, t) \tag{2.10}$$

Since $E_0^2 \propto I$ this means, that the ponderomotive force scales $F_p \propto -\nabla I$. In this case, the pondermotive force expels the electrons in the transverse direction from the laser propagation direction.

2.2 Relativistic interaction and motion of laser pulses with matter

For the intensities of interest the velocities of the accelerated electrons become ultra-relativistic nearing the speed of light ($v_q \approx c$). This comes with the relativistic mass-increase such that Eq. (2.2) transforms to

$$\vec{F} = \frac{d\gamma \vec{p}}{dt} = -e(\vec{E} + \frac{\vec{v}}{c} \times \vec{B}), \tag{2.11}$$

for a electron with the *Lorentz factor* γ

$$\gamma = \frac{1}{\sqrt{1 - \frac{v^2}{c^2}}}. \tag{2.12}$$

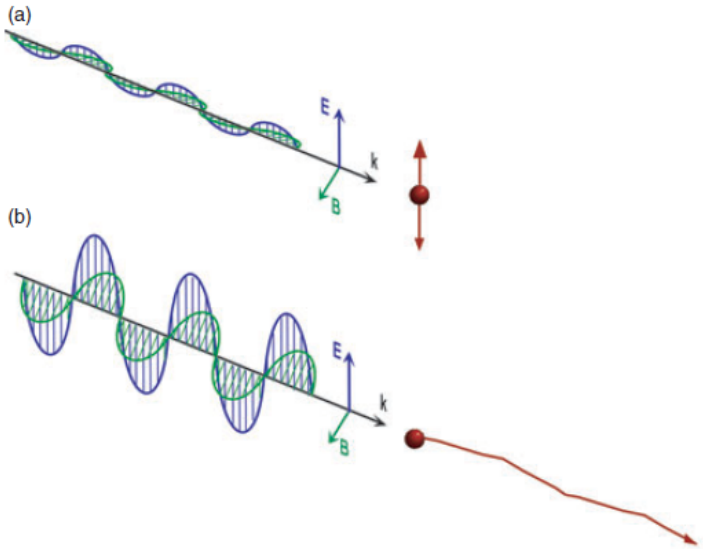

Figure 2: Visualization of the motion of an electron in a laser's electromagnet wave. a) shows the classical case ($v \ll c \Rightarrow a_0 \ll 1$). The light amplitude is small and the electron follows the electric field's polarization at the laser's frequency. There is no deviation from the laser's propagation axis $\hat{k}$ in the electron's motion. b) gives the ultra-relativistic case ($v \approx c \Rightarrow a_0 \gg 1$). The light's amplitudes are significantly larger, such that the magnetic field exerts a force on the electron that has to be taken into account.[24]

In this case the electron's momentum exceeds $m_e c$, with m_e being the electron's rest mass. This means the electron's mass virtually increases of a factor γ. It's relativistic mass m_e' is given by

$$m_e' = \gamma m_e. \tag{2.13}$$

In this regime it is common to introduce the dimensionless scaling variable a_0 [24]

$$a_0 \equiv \frac{v_t}{c} = \frac{eE_0}{\omega m_e c}, \tag{2.14}$$

the so called *normalized laser amplitude* [10]. In this case v_t describes the electrons transverse speed to the pulse's k-vector. This scaling variable a_0 can be understood as normalized vector potential corresponding to the classical velocity of a freely moving electron oscillating in a linearly polarized (LP) electric laser field [11]. To put this into perspective, this is given in practical units

$$a_0 = 0.85 \times 10^{-9} \lambda[\mu\text{m}] \sqrt{I_L[\text{W/cm}^2]}. \tag{2.15}$$

When $a_0 \simeq 1$, which is correct for $\lambda^2 I_L \gtrsim 10^{10}\,\text{W}$ for a $\lambda = 1\,\mu\text{m}$ laser with a focused intensity of $I_L \gtrsim 1.38 \times 10^{18}\,\text{W/cm}^2$, dynamics become nonlinear and the electrons virtual mass m_e' increases drastically in comparison to m_e. With laser intensities exceeding $10^{22}\,\text{W/cm}^2$ the relevant dynamics considered here are nearly ultra-relativistic with $a_0 \gg 1$. Practically one can retrieve the electromagnetic

field strengths with the help of a_0:

$$E_0 = \frac{a_0}{\lambda[\mu\mathrm{m}]} 32.2\,\mathrm{GV\,cm^{-1}} \tag{2.16}$$

$$B_0 = \frac{E_0}{c} = \frac{a_0}{\lambda[\mu\mathrm{m}]} 10.7\,\mathrm{kT}. \tag{2.17}$$

Additionaly a_0 gives a simple way to calculate the peak intensity I_0 of the lasers pulse with the help of

$$I = \frac{c\epsilon_0}{2} E^2 \tag{2.18}$$

$$I_0 \approx \frac{a_0^2}{\lambda^2[\mu\mathrm{m}^2]} 1.37 \times 10^{18}\,\mathrm{W/cm^2}. \tag{2.19}$$

Analogous to Eq. (2.11) the ponderomotive force Eq. (2.9) transforms to:

$$F_p = -\frac{e^2}{4\langle\gamma\rangle m_e \omega^2} \nabla E_0^2(\vec{r}, t), \tag{2.20}$$

Where $\langle\gamma\rangle$ is the characteristic relativistic γ-factor averaged over a cycle of the electrons motion within the laser-pulses EM wave. Due to it's definition Eq. (2.14), we can estimate $\langle\gamma\rangle$ as

$$\langle\gamma\rangle \approx \sqrt{1 + a_0^2}. \tag{2.21}$$

Thanks to a_0 we can shorten the relativistic ponderomotive force's expression Eq. (2.20) to:

$$F_p = -\frac{m_0 c^2}{4\langle\gamma\rangle} \nabla a_0^2. \tag{2.22}$$

Now we can approximate the characteristic avaraged γ-factor of the electrons $\langle\gamma\rangle$ in the limit of $a_0 \gg 1$ to be $\langle\gamma\rangle \approx a_0$ [10], which enables us to simplify Eq. (2.22) even further, while keeping in mind that all fields and therefor a_0 as well are functions of space and time as described at the end of the previous section ($a_0 \longrightarrow a_0(\vec{r}, t)$):

$$F_p(\vec{r}, t) \approx -\frac{m_0 c^2}{4} \nabla a_0(\vec{r}, t). \tag{2.23}$$

2.3 Radiation reaction

When a charged particle is accelerated within an electromagnetic field it emits so called *synchrotron radiation* tangential to its momentum. The synchrotron power emission P_{sync} then is exclusively defined by the particles acceleration in its instantaneous rest frame. For a electron with mass m_e, velocity $\vec{v}$, Lorentz-factor γ and charge $|e|$, the emitted power P_{sync} is proportional to:

$$\boxed{\eta \equiv \frac{\gamma}{E_s} \sqrt{\left(\vec{E} + \frac{1}{c}\left(\vec{v} \times \vec{B}\right)\right)^2 - \frac{1}{c^2}\left(\vec{E}\vec{v}\right)^2},} \tag{2.24}$$

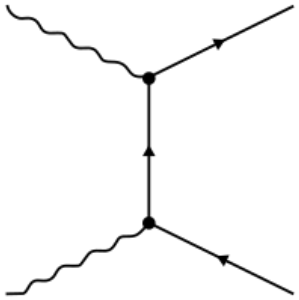

Figure 3: Feynman diagram of the *linear Breit-Wheeler-Process*. Two high-energy photons collide and create a electron-positron-pair under the exchange of a virtual positron.

Here $\vec{E}$ and $\vec{B}$ are the incident lasers electric and magnetic fields. $E_s \approx 1.3 \times 10^{18}\,\mathrm{V\,m^{-1}}$ is the so called *Schwinger limit* or *Schwinger field*, which defines the field strength at which quantum electrodynamic (QED) effects become important [10]. Additionally one could consider the radiation emission due to *Bremsstrahlung* released due to the electron's motion within the ion's vicinity, but this effect does not create such copious amounts of high-energy multi-MeV γ-photons as the synchrotron radiation.

There are two reactions of high interest besides the emission of synchrotron radiation, the *nonlinear inverse Compton scattering* and the so called *Breit-Wheeler process* of e^-e^+-pair production. The process of *nonlinear inverse Compton scattering* describes how a highly relativistic electron collides with a incident photon and transfers energy to it. This increase in photon energy can have a maximum value equal to the electron's kinetic energy [7, 19]. The *Breit-Wheeler process* (BWP) in turn is the process of two high-energy photons colliding and creating an electron-positron-pair. It has to be differentiated between the linear and the nonlinear BWP. The linear BWP is the "prototype" of the fundamental process and is visualized by the Feynman-graph in Fig. 3. The linear BWP has not been observed in laboratories but is especially important in astrophysics [10]. In comparison the nonlinear BWP includes more then two photons per collision. In general for both BWPs there is a very low cross-section and a high energy threshold for the collisions required [7, 10, 27].

3 Laser pulse propagation within plasma target

3.1 Relativistic Transparency and self-focusing

For a plasma the optical properties are dictated by it's electron density n_e [10].
In the classical regime a laser is able to propagate through a plasma up until the so called *critical density* n_{cr} (sometimes called *cutoff density*) [10, 24]:

$$n_{cr} \equiv \frac{m_e \omega^2}{4\pi e^2}. \tag{3.1}$$

This means, that if the electron density $n_e \geq n_{cr}$, the plasma is *over-dense* and turns opaque for the laser and its propagation is inhibited. In the case of ultra-relativistic electrons ($a_0 \gg 1$) the relativistic mass increase of the electrons mass m_e (Eq. (2.13)) has to be taken into account with the afore defined characteristic relativistic Lorentz-factor $\langle\gamma\rangle$. Together with the approximation $\langle\gamma\rangle \approx a_0$ introduced in Section 2.2 the plasma will stay transparent for an ultra-strong laser-pulse if

$$n_e < a_0 n_{cr}. \tag{3.2}$$

This effect is called *relativistic transparency* and enables a ultra-strong laser to propagate through a classically opaque plasma. In other words, the critical density n_{cr} is the plasma density when the laser's frequency ω is equal to the *plasma frequeny* ω_p. The plasma frequency ω_p is the frequency in which the plasma's electrons vibrate due to the electromagnetic forces between them and the ions. In the non-relativistic case it is defined as [24]:

$$\omega_{p0} \equiv \sqrt{\frac{4\pi n_e e^2}{m_e}}, \tag{3.3}$$

With m_e being the electron's rest mass and e the elementary charge. It needs to be recognized, that for this calculation the ions mass was approximated as $m_i \to \infty$ ($m_i \gg m_e$). This approximation is still valid for the considered H-plasma consisting only out of electrons and protons since $m_e/m_p \ll 1$.
As before for highly relativistic electrons, their mass increase has to be considered such that the plasma frequency ω_p is written as:

$$\omega_p \equiv \frac{\omega_{p0}}{\sqrt{\gamma}}, \tag{3.4}$$

Here γ is again the electron's Lorentz-factor. This change in the plasma frequency further introduces changes in the plasma's dielectric properties by modifying it's refractive index n experienced by the laser, which is given by

$$n = \sqrt{1 - \left(\frac{\omega_p}{\omega}\right)^2} \tag{3.5}$$

Due to the spatial profile, introduced in Section 2.1, of the laser's wavefront the electron's Lorentz-factor becomes a function of position and time, i.e $\gamma \to \gamma(r,t)$, where r is the radial distance to the laser's axis of propagation $\hat{k}$. This in turn makes the refractive index n become space and time dependent as well, $n \to n(r,t)$. Since we are considering the laser's wavefront to have Gaussian distribution with it's maximum on axis, we expect $n(r,t)$ to show a similar form with a maximum along the lasers propagation axis ($n(0) \geq n(r)$).
This effects the lights phase velocity $v_\phi = \frac{c}{n}$. With increasing radial distance r to the laser's axis of propagation $\hat{k}$ this increases the lights phase speed such that $v_\phi(0) \leq v_\phi(r)$. Due to these nonliear changes in n the wavefront is curved inwards and is making the laser converge on itself, introducing the so called effect of *relativistic self-focusing* [1, 15, 23, 24]

In the here considered regime the diffraction index n is dependent of the incident laser intensity I as

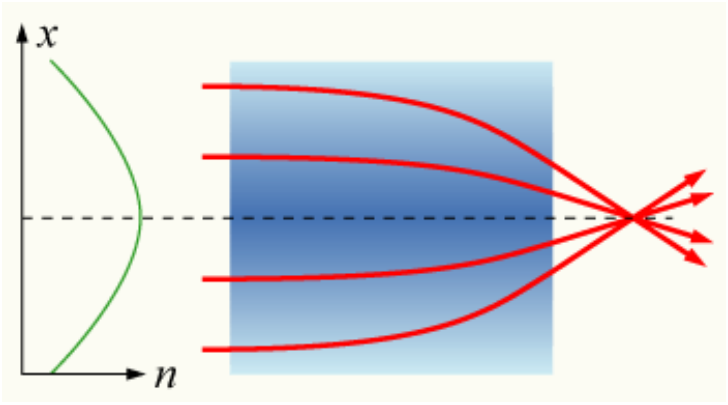

Figure 4: Schematic visualization of the *relativistic self-focusing* effect. Spatial change of the plasma's diffraction index n and it's effect on the laser's wavefront's propagation axes [25]

is noticeable in Eq. (3.5) and Eq. (3.4) due to $w_p \propto \gamma^{-1/2}$. This nonlinear intensity dependency can be approximated as:

$$n \approx n_0 + n_2 I. \tag{3.6}$$

Here n_0 is the classical linear refractive index introduced in Eq. (3.5) and n_2 the nonlinear contribution to the total refractive index. In the relativistic case, there is a critical power P_{cr} which the laser has to exceed to experience this effect [15, 23]:

$$P_{cr} = \frac{m_e c^5 \omega^2}{e^2 \omega_p} \simeq 17\,\mathrm{GW} \left(\frac{\omega}{\omega_p}\right)^2 \tag{3.7}$$

This critical power P_{cr} is greatly exceeded by the here considered lasers with powers exceeding 1 PW.

3.2 Laser envelope model

A laser pulse can simply be described by its *vector potential* A (in this section we will refrain the use of vector arrows to prevent confusion), which is the non-normailzed form of a_0 introduced in Section 2.2 (Eq. (2.14)) in the form:

$$|A| = \frac{m_e c a_0}{e}. \tag{3.8}$$

This also implies $|A| = E_0/\omega$ as well as $|A| = B_0 c/\omega$ according to Eq. (2.17). In general A defines the pulse's electric field as

$$\vec{E} = -\frac{\partial \vec{A}}{\partial t}. \tag{3.9}$$

Since the phenomena of interest are rather in the scale of λ_p (Eq. (3.4)) then the laser's wavelength λ_0 one can simplify the description of the pulse by using a *complex envelope* $\tilde{A}$ assuming that A is built

from a slowly varying part $\bar{A}$ and a fast oscillating part $\hat{A}$ like

$$A = \bar{A} + \hat{A}. \tag{3.10}$$

The quickly oscillating component $\hat{A}$ can then be described as the real part of a slowly varying complex envelope $\tilde{A}$ modulated by fast oscillations at scales of λ_0 moving at the speed of light c:

$$\hat{A}(r,t) = \mathrm{Re}\left[\tilde{A}(r,t)e^{i(k_0 x - \omega_0 t)}\right], \tag{3.11}$$

where $k_0 = 2\pi/\lambda_0$. In this case "slowly varying" refers to the temporal and spatial changes (∂_t and ∂_r) of $\bar{A}$ and $\hat{A}$ being very small and treatable as perturbations. Analogously to Eq. (3.9) $\hat{A}$ defines the quickly oscillating component of the pulse's electric field as:

$$\hat{E} = -\partial_t \hat{A} = \mathrm{Re}\left[\tilde{E}(r,t)e^{i(k_0 x - \omega_0 t)}\right], \tag{3.12}$$

where $\tilde{E}(r,t)$ is the electric field's complex envelope given as:

$$\tilde{E} = -(\partial_t - ik_0 c)\tilde{A}(r,t). \tag{3.13}$$

This enables us to describe the pulse's evolution by using the well known *envelope equation* [3]

$$\nabla^2 A - \frac{1}{c^2}\partial_t^2 A = -\frac{4\pi}{c} j_t, \tag{3.14}$$

where j_t is the transverse current density given by

$$j_t = -n_{ch} e v_t = -\frac{n_{ch} e p_t}{m_e \gamma}. \tag{3.15}$$

Here n_{ch} is the channel's electron density, v_t and p_t the electrons transverse speed nd momentum and γ their relativistic Lorentz-factor. Assuming a circularly polarized (CP) laser in 1D, we can aproximate p_t as

$$p_t = \frac{eA}{c}. \tag{3.16}$$

With this approximation, which is only true for CP laser pulses in the mildly relativistic regime, we can simplify Eq. (3.14) to

$$\nabla^2 A - \frac{1}{c^2}\partial_t^2 A = -\frac{\omega_p^2}{\gamma c^2} A. \tag{3.17}$$

Here $\omega_p = \sqrt{\frac{4\pi n_{ch} e^2}{m_e}}$ is the plasma frequency (Eq. (3.4)). One can also tell from Eq. (3.16) that the local Lorentz-factor γ can also be written as

$$\gamma = \sqrt{1 + \frac{e^2 A^2}{m^2 c^4}}. \tag{3.18}$$

We now assume the pulse to have an envelope like $\tilde{A} = \frac{1}{2}A_0$,

$$A = \frac{1}{2}A_0(y,x,t)e^{i(k_0x-\omega_0t)} + c.c., \tag{3.19}$$

with $A_0 = |A|$. In the 2D Cartesian-coordinates used, the y-axis corresponds to the radial axis r in 3D cylindrical coordinates along the lasers propagation axis $\hat{k}$ along the x-axis, which is why later on we will understand ∂_y as the perpendicular gradient $\nabla_\perp$. The complex envelope $A_0(y,x,t)$ is slowly varying as explained above:

$$|\partial_x A_0| \ll k_0 A_0, \tag{3.20}$$

$$|\partial_t A_0| \ll |\omega_0 A_0|\,, \tag{3.21}$$

which enables us to apply the so called *WKB-approximation* (Wentzel–Kramers–Brillouin) [13]. If we assume A_0 to be constant this then yields together with Eq. (3.17) the well known dispersion relation

$$\boxed{\omega_0^2 = \frac{\omega_p^2}{\gamma_0} + k_0c^2,} \tag{3.22}$$

with

$$\gamma_0 = \sqrt{1 + \frac{e^2A_0^2}{2m_e^2c^4}}, \tag{3.23}$$

as the linear Lorentz-factor according to Eq. (3.18). In reality A_0 is not constant but slowly varying. To account for this in our solution of Eq. (3.17) we calculate $\nabla^2 A$ as

$$\nabla^2 A = \frac{1}{2}\nabla^2\left[A_0(y,x,t)e^{i(k_0x-\omega_0t)} + c.c.\right] = \frac{1}{2}\left[\partial_y^2 A_0 + 2ik_0\partial_x A_0 - k_0^2 A_0\right]e^{i(k_0x-\omega_0t)} \tag{3.24}$$

and similarly for $\partial_t^2 A$

$$\partial_t^2 = \frac{1}{2}\partial_t^2\left[A_0(y,x,t)e^{i(k_0x-\omega_0t)} + c.c.\right] = \frac{1}{2}\left[-2i\omega_0\partial_t A_0 - \omega_0 A_0\right]e^{i(k_0x-\omega_0t)}, \tag{3.25}$$

ignoring second order derivatives along the propagation axis $\hat{k} = \hat{x}$. We insert these two forms into Eq. (3.17) and simplify this to

$$\nabla_\perp A_0 + 2ik_0\partial_x A_0 - k_0 A_0 + \frac{2i\omega_0}{c^2}\partial_t A_0 + \frac{\omega_0^2}{c^2}A_0 = \frac{\omega_p^2}{\gamma^2}A_0. \tag{3.26}$$

Applying the dispersion relation (Eq. (3.22)) we finally yield an envelope model describing a pulse propagating through a plasma by

$$\boxed{2i\omega_0\partial_t A_0 + c^2\nabla_\perp A_0 + \frac{\omega_p^2}{\gamma_0^2}A_0^2 = \frac{\omega_p^2}{\gamma}A_0.} \tag{3.27}$$

The left hand side (LHS) of the equation being the planar wave approximation, assuming $A_0 = const$ and the right hand side (RHS) the envelope approximation. It should be especially pointed out how the RHS Lorentz-factor is not γ_0 but the local electron Lorentz-factor as introduced in Eq. (3.18).

3.3 Dynamic filamentation instability

A laser pulse propagating in a uniform plasma or a plasma is susceptible to *dynamic filamentation instability*. This filamentation instability of a laser pulse occurs due to variation of refractive index n (Eq. (3.6)) either due to the pondermotive force or the relativistic mass variation of electrons in a direction perpendicular to the laser propagation [12]. Consequently, the phase velocity of the laser pulse varies along its wavefront, bending it in the transverse direction, resulting in the laser branching out in several filaments. This phenomenon is comparable to small turbulent flows within a larger laminar flow in hydrodynamics. Due to their high intensities these filaments drive strong electron acceleration enhancing γ-photon emission. For a Gaussian laser pulse propagating in a plasma, both ponderomotive force induced cavitation and relativistic mass variation of the electrons across the laser wavefront cause the filamentation and affect the laser filament size. However, for a laser pulse propagating in a plasma channel, the relativistic mass nonlinearity dominates over the ponderomotive force nonlinearity [21]. To understand the filaments behaviour, especially their growth and size, some calculations have been done on the basis of previous calculations [13]. Ignoring the effect of the pondermotive force induced cavitation of the plasma electrons, the wave equation governing the laser propagation can be written as introduced in Eq. (3.27):

$$2i\omega_0\partial_t A_0 + c^2\nabla_\perp A_0 + \frac{\omega_p^2}{\gamma_0^2}A_0^2 = \frac{\omega_p^2}{\gamma}A_0. \tag{3.28}$$

The laser pulse satisfies the dispersion relation Eq. (3.22) in the plasma. This equation is strictly valid in the mildly relativistic regime. To estimate the size and growth of these filaments we introduce small perturbation in the laser's complex vector potential as $A_0(y,x,t) \rightarrow A_0(x) + \delta A(y,t))$ (Eq. (3.19)), with $\delta A \sim \frac{1}{2}e^{i(q_\perp y - \delta\omega t)} + c.c.$. This perturbation then modulates the electron's Lorentz-factor (Eq. (3.23)), such that

$$\gamma = \left[1 + \frac{e^2}{2m_e^2c^2}\left[A_0^2 + A_0\left(\delta A + \delta A^*\right)\right]\right]^{\frac{1}{2}}. \tag{3.29}$$

In this case δA^* represents the complex conjugate of δA. We can rewrite the Lorentz factor into a linear part equal to Eq. (3.23) and a nonlinear component:

$$\frac{1}{\gamma} = \frac{1}{\gamma_0}\left[1 + \frac{e^2}{2m_e^2c^2\gamma_0^2}A_0\left(\delta A + \delta A^*\right)\right]^{\frac{1}{2}}, \tag{3.30}$$

which can be further simplified by binomial expansion

$$\frac{1}{\gamma} = \frac{1}{\gamma_0} - \frac{e^2}{4m_e^2c^2\gamma_0^3}A_0\left(\delta A + \delta A^*\right). \tag{3.31}$$

Inserting this form for the Lorentz-factor γ into the envelope model Eq. (3.27), gives the wave equation for transverse perturbations considering the electrons relativistic mass increase

$$\boxed{2i\omega_0\ \partial_t \delta A^* + c^2\nabla_\perp^2 \delta A + \frac{\omega_p^2 a_0^2}{4\gamma^3}\left(\delta A + \delta A^*\right) = 0,} \tag{3.32}$$

where $a_0 = e^2A_0^2/m^2c^4$ is the laser's normalized vector potential and ω_p the plasma frequency (Eq. (3.4)). To further analyse this wave equation we separate the imaginary and real parts of the complex perturbation $\delta A = \delta A^r + i\delta A^i$, with δA^r, $\delta A^i \sim \frac{1}{2}e^{i(q_\perp y - \delta\omega)}$, to yield

$$-2\omega_0\partial_t\delta A^i + c^2\nabla_\perp^2\delta A^r + \frac{\omega_p^2 a_0^2}{4\gamma_0^3}\delta A^r = 0, \tag{3.33}$$

$$2\omega_0\partial_t\delta A^r + c^2\nabla_\perp^2\delta A^i o = 0, \tag{3.34}$$

which represent the real and imaginary part of the complex wave function Eq. (3.32). By linearizing for δA^r and δA^i respectively we obtain

$$\left(-q_\perp^2c^2 + \frac{\omega_p a_0^2}{2\gamma_0^3}\right)\delta A^r = -2i\omega_0\delta\omega\delta A^i, \tag{3.35}$$

$$-c^2q_\perp^2\delta A^i = 2i\omega_0\delta\omega\delta A^r. \tag{3.36}$$

Multiplying these two equation we yields the squared perturbation of the laser frequency

$$\delta\omega^2 = -\frac{c^2q_\perp^2}{4\omega_0^2}\left[\frac{\omega_p^2a_0^2}{2\gamma_0^3} - c^2q_\perp^2\right]. \tag{3.37}$$

With this we finally obtain the growth rate, $\Gamma = \mathrm{Im}(\delta\omega)$, of the filamentation instability as

$$\boxed{\Gamma = \frac{q_\perp^2c^2}{4\omega_0^2}\left[\frac{\omega_p^2a_0^2}{2\gamma_0^3} - q_\perp^2c^2\right]^{1/2}.} \tag{3.38}$$

This equation gives the filament size as $q_\perp^{-1} = (c/\sqrt{2}\omega_p)a_0$ [13]. Thus, for the channel width or the laser spot size exceeding the filament size $q_\perp^{-1}$, one can expect strong filamentation of the laser pulse, resulting in the loss of efficiency in high-energy photons production. For the parameters $a_0 = 190, n_{\mathrm{ch}} = 20$, this size turns out to be $\sim 4\,\mu\mathrm{m}$ which is consistent with PIC simulations results. It should be pointed out that the analytical calculations, though being derived for the mildly relativistic regime, give a very good scaling for the ultra-relativistic parameter of the PIC simulations. This can be due to the self-similarity of the plasma processes, (arising in this case due to relativistic mass transparency effects) that facilitate the comparison of the filamentation instability in two different parameters regimes. In addition to this the primary approximations are only true for CP laser pulses but are applicable due to the same

self-similarity to the here used LP laser by correcting the normalized vector potential by a factor of $\sqrt{2}$

$$a_0^{LP} = \frac{a_0^{CP}}{\sqrt{2}}. \tag{3.39}$$

3.4 Target geometry

Recently it has been shown that a structured target can greatly enhance multi-MeV γ-photon emission and improve the collimation of resulting beams by guiding the high-energy photons [9, 10, 22, 28]. The simplest case for such a structured target is a so called *plasma channel*. As the name suggests it consist of a bulk target with a lower density cylindrical channel along it's center axis. The bulk of a target has to be of a near critical electron density (NCD) $n_e = n_B \lesssim a_0 n_{cr}$ (Eq. (3.2) and Eq. (3.1)) to be able to offer the laser pulse adequate guiding. The channel however has to be of considerably lower electron density $n_e = n_{ch} \ll a_0 n_{cr}$ to allow the laser pulse to propagate through the effect of relativistic transparency but also enable efficient energy conversion [22]. It has been shown that for optimal collimation and high energy γ-photon generation the optimal channel density for a laser with $a_0 \approx 190$ is given at roughly $n_{ch}/n_{cr} = 20$ [10]. In comparison at lower densities the total number of emitting electrons is greatly reduced, and the propagation of the pulse is significantly deteriorated at higher densities even though the total flux of generated high energy γ-photons is increased. In addition to providing guidance for the laser pulse, a structured target like this can also greatly enhance the generation of multi-MeV γ-photons as a result of the generation of strong quasi-static azimuthal magnetic fields created due to strong relativistic electron currents driven by direct laser acceleration. In the case of a 2D simulation the azimuthal axis from 3D cylindrical coordinates is equal to the z-axis $\hat{e_z}$ in 2D cartesian coordinates. When the laser pulse hits the plasma channel, it accelerates electrons to ultra-relativistic energies as explained in Section 2.2. This drives strong longitudal electron currents along the laser's propagation axis $\hat{k}$, which in turn create a slowly evolving quasi-static azimuthal magnetic field B_z (Here z is used since the simulations carried out are in 2D cartesiasn coordinates and as such the z-axis corresponds to the 3D cylindrical azimuthal axis). The spatial gradient of the laser wavefront intensity further accumulates these electrons towards the edge of the plasma channel, where they interact with the outer part of the bulk plasma experiencing strong acceleration forces as they come to halt and release energy as high-energy synchrotron photons, maximizing η, before getting accelerated again [9] (Section 2.3). The resulting trajectory of the plasma electrons can be described as zigzag motion from one side of the channel to the other along $\hat{k}$ (Fig. 5). Even though the plasma's magnetic field does not carry out any work on the electrons it alters their emission behaviour. One can easily tell from Eq. (2.24) how a present strong magnetic field can enhance the power of emitted γ-photons in this process. The required strength of these quasi-static magnetic fields B_z to significantly enhance radiation power η is given by a critical value of:

$$B_{z,crit} \approx \frac{B_0}{a_0^2}, \tag{3.40}$$

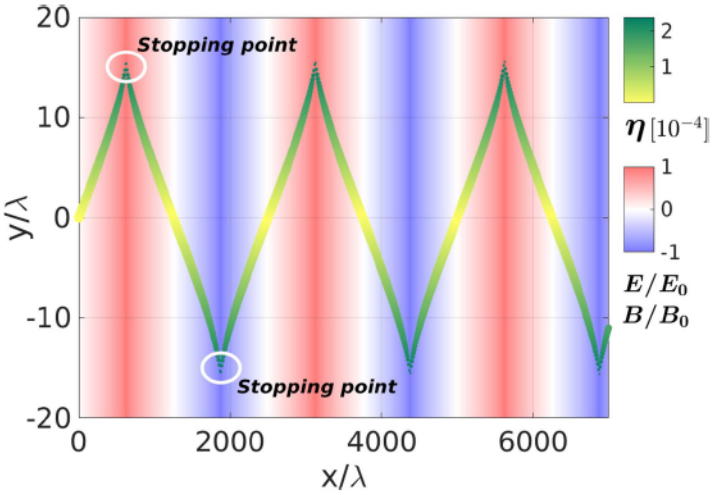

Figure 5: Trajectory of an electron within a planar polarized laser with a normalized amplitude of $a_0 = 100$. The red and blue background colours suggest the laser's field strength normalized to thei maximum value.The colour of the electron trajectory visualizes η (Eq. (2.24)), the size of the trajectory represents the change in the electron's γ-factor [9].

here B_0 gives the incident laser's magnetic field strength and a_0 is the normalized laser amplitude (Eq. (2.14)). Since $a_0 \gg 1$ this means that even for much lower laser amplitudes then B_0 these plasma-fields can enhance an electrons emission power η. Simulations suggest that these plasma fields reach field strengths in magnitudes of up to orders of MT, resulting in greatly enhanced γ-photon powers [9]. We can also estimate the maximum possible magnetic fieldstrength B_z for such currents

$$B_{z,max} = \frac{4\pi}{c} e n_e c R \approx 6 \times 10^5 \text{ T}, \tag{3.41}$$

where n_e is the channel's electron density and R is the channel radius. This estimation assumes that all electrons within the channel initially are accelerated to the speed of light within the channel, creating the current to drive an azimuthal magnetic field comparable to a current running through a straight wire [22].

3.5 Simulation method

The main task of the simulations carried out is to find if there is a critical power of the incident laser pulse, P_L at which the generation of high-energy radiation becomes saturated for a fixed target electron density and incident laser intensity I_0 (Eq. (2.19)). For this the energy conversion efficiency ϵ of the pulse's power into radiation is observed.

$$\epsilon = \frac{E_{rad}}{E_{laser}}. \tag{3.42}$$

In addition the quality of collimation of the generated high-energy γ-photon beam is determined. For this the open source PIC (particle in cell) code SMILEI [4] was used. The PIC method was initially developed for fluid dynamic studies in the 1960s and is greatly regarded for its conceptual simplicity

and efficiency in parallel computing. Today, plasma physics strongly rely on such PIC simulations. For these PIC-codes the distribution of charged plasma particles becomes discretized into sums of so called "macro-particles" (or "quasi-particles") N_s, for each species s of particles:

$$f_s(t,\vec{x},\vec{p}) = \sum_{p=1}^{N_s} w_p S(\vec{x}-\vec{x}_p(t))\delta(\vec{p}-\vec{p}_p(t)), \tag{3.43}$$

where w_p is the quasi-particles "weight", $\vec{x}_p$ its position, $\vec{p}_p$ its momentum and $S(\vec{x})$ the shape-function of all macro particles. The shape-function $S(\vec{x})$ used in SMILEI is given in Appendix A of [4]. In addition to their specific wheight these macro-particles carry a specific charge q_s. All the macro particles follow the relativistic equation of motion (compare to Eq. (2.11))

$$\frac{d\vec{x}_p}{dt} = \frac{\vec{u}_p}{\gamma_p}, \tag{3.44}$$

$$\frac{d\vec{u}_p}{dt} = r_s(\vec{E}_p + \frac{\vec{u}_p}{\gamma_p} \times \vec{B}_p), \tag{3.45}$$

here $r_s = q_s/m_s$ is the species specific charge-over-mass ratio and $\vec{u}_p = \vec{p}_p/m_s$ the p^{th} macro particle's reduced momentum and the electromagnetic fields interpolated at the p^{th} particle's position

$$\vec{E}_p = \int d\vec{x}\ \ S(\vec{x}-\vec{x}_p)\vec{E}(\vec{x}), \tag{3.46}$$

$$\vec{B}_p = \int d\vec{x}\ \ S(\vec{x}-\vec{x}_p)\vec{B}(\vec{x}). \tag{3.47}$$

With the position and momentum given for all particles, as well as the electromagnetic fields at their position for a timestep n, the code uses a second order leap-frog integrator to calculate the particles new momentum:

$$\vec{u}_p^{(n+\frac{1}{2})} = \vec{u}_p^{(n-\frac{1}{2})} + r_s\Delta t\left[\vec{E}_p^{(n)} + \frac{\vec{v}_p^{(n+\frac{1}{2})} + \vec{v}_p^{(n-\frac{1}{2})}}{2} \times \vec{B}_p^{(n)}\right], \tag{3.48}$$

to than compute the particles new position at the timestep $n+1$:

$$\vec{x}_p^{(n+1)} = \vec{x}_p^{(n)} + \Delta t\frac{\vec{u}_p^{(n+\frac{1}{2})}}{\gamma_p}, \tag{3.49}$$

where Δt is the timestep duration and $\vec{E}_p^{(n)}$ and $\vec{B}_p^{(n)}$ the electromagnetic fields interpolated at the particles position at the n^{th} timestep. The current density $\vec{j}$ is than calculated analogously by using charge conservation. Knowing the currents the code than computes the electromagnetic fields for the whole simulation by solving *Maxwell's equations*. This computation for the electromagnetic fields happens on a discrete grid. The space in between the grid points are the cells which give this method its name. In Table 1 a schematic overview of this PIC-loop is given. For our 2D simulation we've chosen a total simulation size of 120×8 µm ($x \times y$) with a cell size of 0.02×0.01 µm simulating a time period of

Initialization	timestep n=0, time t=0
PIC-loop	from timestep n to $n+1$, time $t = (n+1)\Delta t$
i.	Interpolate electromagnetic fields at particle position
ii.	push particles (compute new momentum and position)
iii.	project current onto the grid
iv.	solve Maxwell's equations

Table 1: Schematic overview of a PIC-loop

λ [µm]	a_0	I_0 [W/cm^2]	τ [fs]	n_{ch}/n_{cr}	n_B/n_{cr}
0.8	190	7.7×10^{22}	40	20	100
0.8	350	2.6×10^{23}	10	37	184

Table 2: Table of characteristic values for both simulation setups

$T_{sim} \approx 5000\,\text{fs}$ for $a_0 = 190$ and half as long for $a_0 = 350$, divided into timesteps of $\Delta t \approx 0.02\,\text{fs}$.
The general setup for the simulations was a 0.8 µm (Ti-Sapphire laser) laser pulse hitting a laser channel as described in Section 3.4. In total the experiment was done two times. For the first experiment the laser has a normalized amplitude of $a_0 = 190$. For the channel we chose an electron density of $n_{ch} = 20 n_{cr}$ and for the bulk of the target $n_B = 100 n_{cr}$ which satisfies the conditions set for the electron densities explained in Section 3.4 and were proven to be optimal for such an pulse [22]. The temporal envelope of the pulse was given by a Gaussian distribution with its FWHM $\tau \approx 40\,\text{fs}$, corresponding to an equal duration of the pulse. The second experiment was oriented on the upcoming ELI/Apollon laser systems and featured a normalized amplitude of $a_0 = 350$ and a pulse duration of $\tau \approx 10\,\text{fs}$. For the second experiment the target density was also modified to $n_{ch} = 37 n_{cr}$ and $n_B = 184 = n_{cr}$ to accommodate for the increase in intensity. As described in Section 2.1 the pulse has an additional spacial intensity profile which was also defined by a Gaussian distribution. The pulse was focused on the center of the channel's opening at $x = 10\,\mu\text{m}$ and $y = 4\,\mu\text{m}$. To maximize energy conversion the waist of the pulse w_0 in the focal plane was chosen to be equal to the channels radius $w_0 = R$. To then realize a power sweep we incrementally increased the pulses waist and the channel's radius to achieve the desired incident power

$$P_L = \pi w_0^2 I_0 = \pi R^2 I_0. \tag{3.50}$$

An overview of all the parameters used is given in Table 2. For both setups a power sweep was done for values of $P_L = 1$, 5, 10, 20, 30 and 40 PW respectively.

4 Simulation Results

4.1 Electron density evolution

To begin with, first we need to understand the evolution of the channel's electron density. For this we take a look at the simulation for $a_0 = 190$ with incident power $P_L = 1\,\mathrm{PW}$. As visible in Fig. 6 (a),

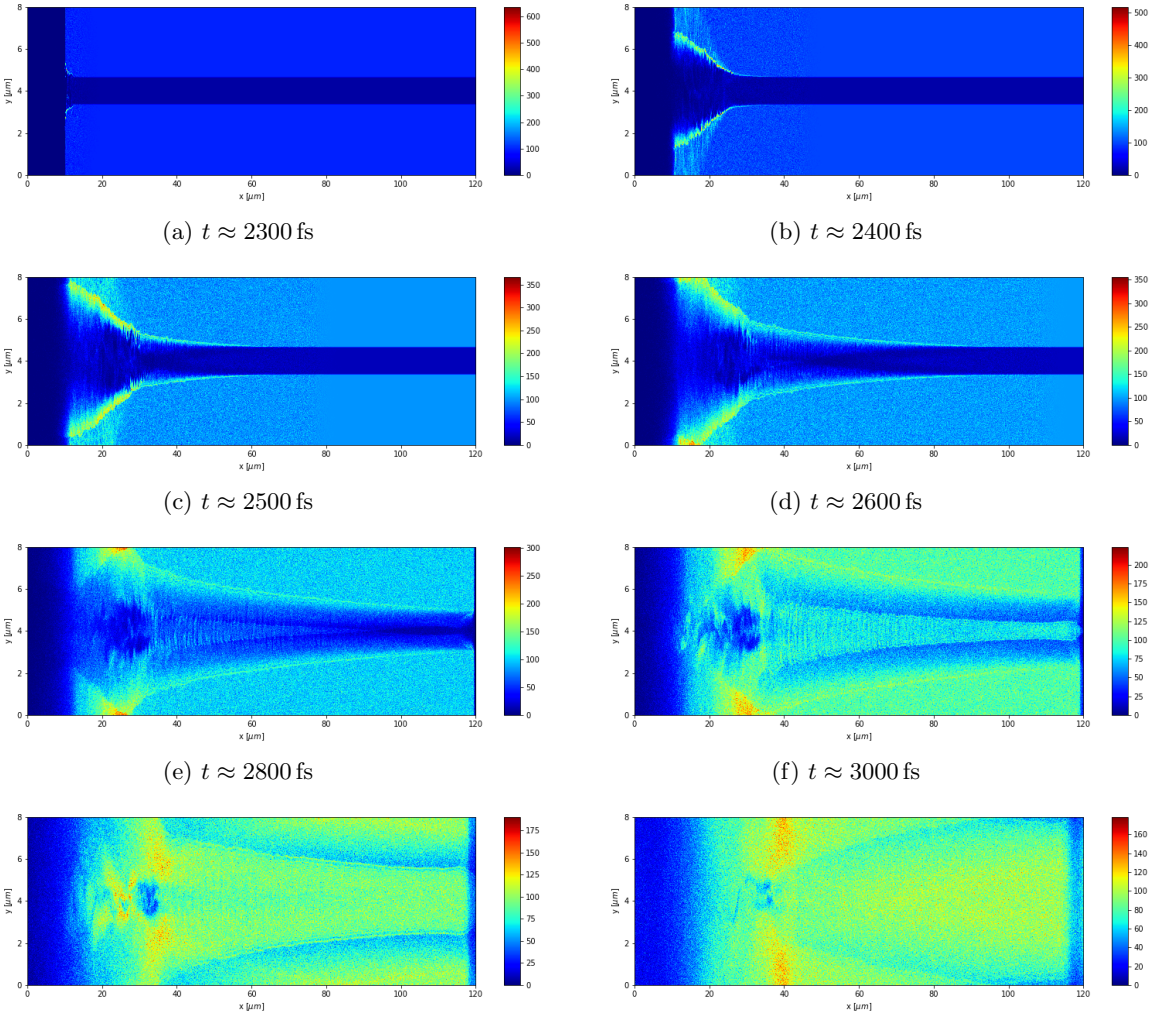

(a) $t \approx 2300\,\mathrm{fs}$ (b) $t \approx 2400\,\mathrm{fs}$

(c) $t \approx 2500\,\mathrm{fs}$ (d) $t \approx 2600\,\mathrm{fs}$

(e) $t \approx 2800\,\mathrm{fs}$ (f) $t \approx 3000\,\mathrm{fs}$

(g) $t \approx 3400\,\mathrm{fs}$ (h) $t \approx 4000\,\mathrm{fs}$

Figure 6: Electron density in units of n_{cr} for given times of a plasma channel being hit with a $a_0 = 190$, $\tau \approx 40\,\mathrm{fs}$ laser pulse with incident power $P_L = 1\,\mathrm{PW}$.

the laser pulse, with Gaussian spatial profile, hits the channel shortly after half of the simulation time T_{sim} has passed. The pulse accelerates most of the channels material out of its way (ponderomotive force expulsion) to the sides, thus regions of high electron densities up to $n_e/n_{cr} \approx 600$ are created. This phenomenon takes place along the total length of the channel but increasingly with the lower strength as the pulse looses its energy through absorption by the electrons and the ions as well. This deforms the channel from its cylindrical shape into a cone with its apex at the right hand side of the channel. From the pulse's initial impact a density shock front (at the border of the plasma channel) is

propagating along the channel. This shock density front is clearly visible from Fig. 6 (c) at the periphery of the plasma channel and beginning of the bulk material. This higher density at the plasma channel boundaries is a result of plasma density compression caused by the ponderomotive force expulsion of the plasma electrons and the return plasma current generation at the channel boundary. Since the laser pulse accelerates a significant amount of the plasma electrons, a return plasma current is generated to compensate the current generated by the accelerated electrons. This system of two opposite plasma currents is unstable and can lead to the filamentation (due to Weibel or current filamentaion instabilities) of the plasma density as later in Fig. 6 (g). After the pulse has mostly been absorbed by the plasma at around $t \approx 2800\,\mathrm{fs}$ more electrons seem to accumulate in the center of the channel again. This happens in a layered manner, where the still widening conical channel has a decreasing density gradient towards the center until in the very center another high density region shaped in the same conical shape as before is formed. Though this channel is much smaller in the transverse direction than than the original plasma channel. In this plasma channel emission of high-energy MeV photons seems to occur. As before, the ponderomotive force expulsion acts on the plasma and the return plasma current generation at the channel boundaries occurs. At this instant, the former plasma channel boundary moves away from the symmetrical axis of the channel until it leaves the simulation window. The inner and denser part of the conical formation keeps expanding unhindered where it can. From the left hand side however the before mentioned shock front mixes the electrons across the whole simulation window width (y-direction) to make it nearly homogeneous in this direction, thus mixing channel and bulk plasmas. However along the x-axis there is still a gradient of electron density rising tail-like up to the shock front. In addition to the current filamentaion and Weibel instabilities, we can observe plasma density oscillations, which can occur due to the mixing of the laser filamentaion and hosing instabilities in the plasma channel [16]. The hosing instability is caused by the plasma's electrons following the polarization of the laser pulse's electric field. These are especially visible in the figures for $t \approx 3000\,\mathrm{fs}$ and later times. On increasing incident power, P_L, we compare the electron density maps for selected times in Fig. 7. On comparing the electron densities visible in Fig. 7 (a), one can see how on increasing the incident power P_L the aforementioned effects of the laser pulse on the plasma motion become more drastic. This means initially the maximum compressed electron density achieved at the plasma channel boundaries increases with P_L, but it drops for $P_L \gtrsim 20\,\mathrm{PW}$, which is noticeable by comparing the colorbar scales for each figure in Fig. 7. In addition the created shock front, which has a Gaussian like form, seems to get wider, e.g. a greater σ-value. This is especially noticeable in part (b) of Fig. 7, where for increasing P_L the shockfront approaches a planar shape. Due to this, one can observe the transition of shock fronts generated by a Guassian laser pulse and a virtually planer laser pulse. Furthermore it looks like, that for all incident powers $P_L \gtrsim 5\,\mathrm{PW}$ the shockfront completely disintegrates the structure of the channel itself, visible in Fig. 7 (b). Again we can clearly see the oscillations of the laser filametation and hosing instabilities, especially for the figure of $P_L = 5\,\mathrm{PW}$ at $t \approx 3000\,\mathrm{fs}$. Furthermore, we can see the first distinct signs of the laser filamentation instabilities in Fig. 7 for $P_L = 40\,\mathrm{PW}$ in front of the shockwave. However it should be

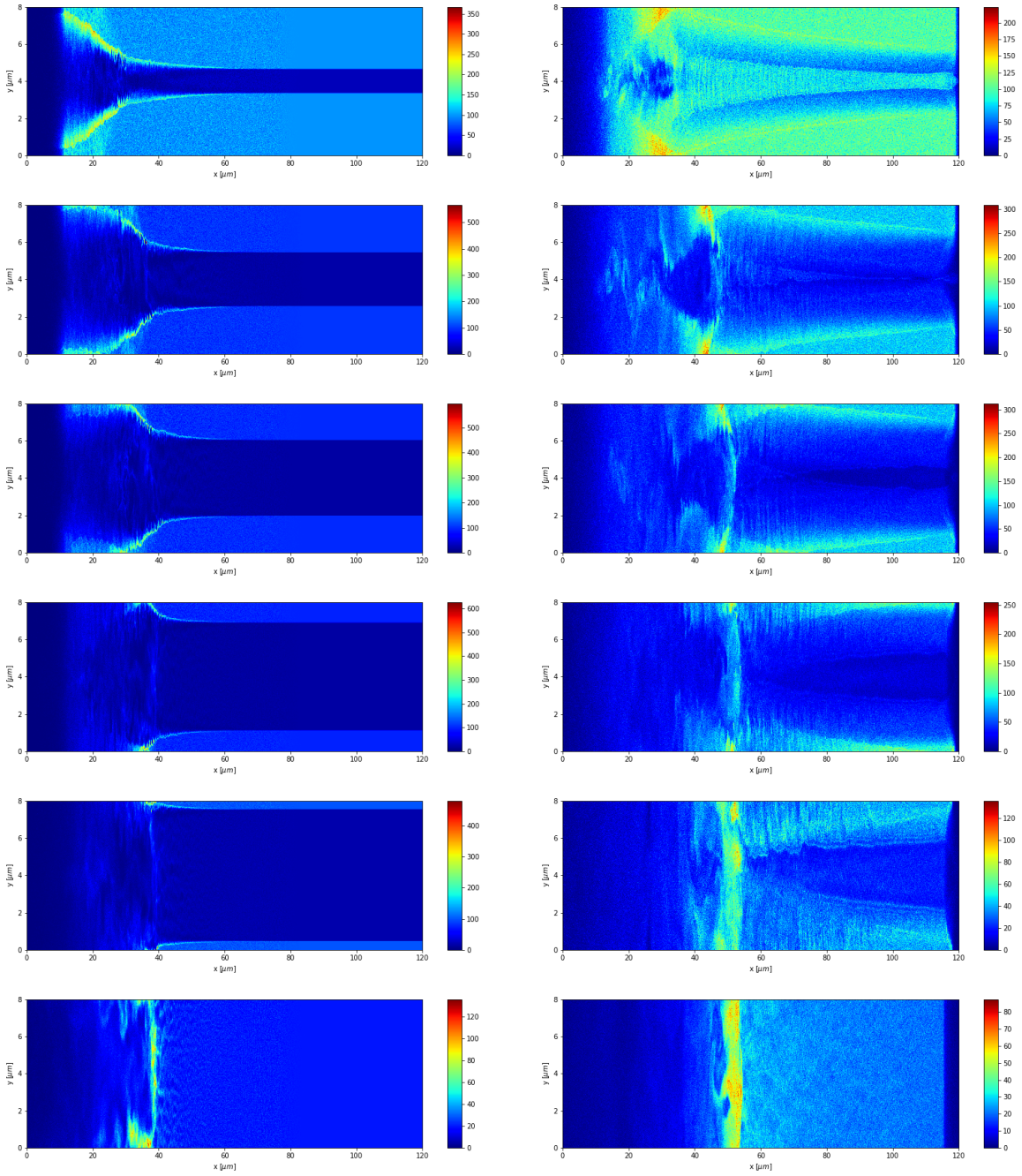

(a) $t \approx 2500\,\mathrm{fs}$ (b) $t \approx 3000\,\mathrm{fs}$

Figure 7: Channel electron densities in units of n_{cr} for simulations of a $\tau \approx 40\,\mathrm{fs}$ laser pulse with normalised amplitude $a_0 = 190$ and incident power $P_L = 1$, 5, 10, 20, 30 and 40 PW (top to bottom) comparison for times a) $t \approx 2500\,\mathrm{fs}$ and b) $t \approx 3000\,\mathrm{fs}$

noted, that this simulation with the parameters $a_0 = 190$ and $P_L = 40\,\mathrm{PW}$ is not representative for a structured target, as the channel radius is larger then the simulation window width along the y-axis. For this reason, results for this simulation are markedly different from the other results. In addition also for $a_0 = 190$, $P_L = 30\,\mathrm{PW}$ the thickness of the bulk plasma is considerably smaller then for lower values of

P_L, which should be kept in mind while evaluating results. We now take a look at the simulations done for a normalized laser amplitude of $a_0 = 350$. Again we show the electron densities n_e of each incident power P_L. For the sake of comparability this will be limited to only two timesteps, representative of the two times shown in Fig. 7 for $a_0 = 190$. The most obvious difference between the simulations for

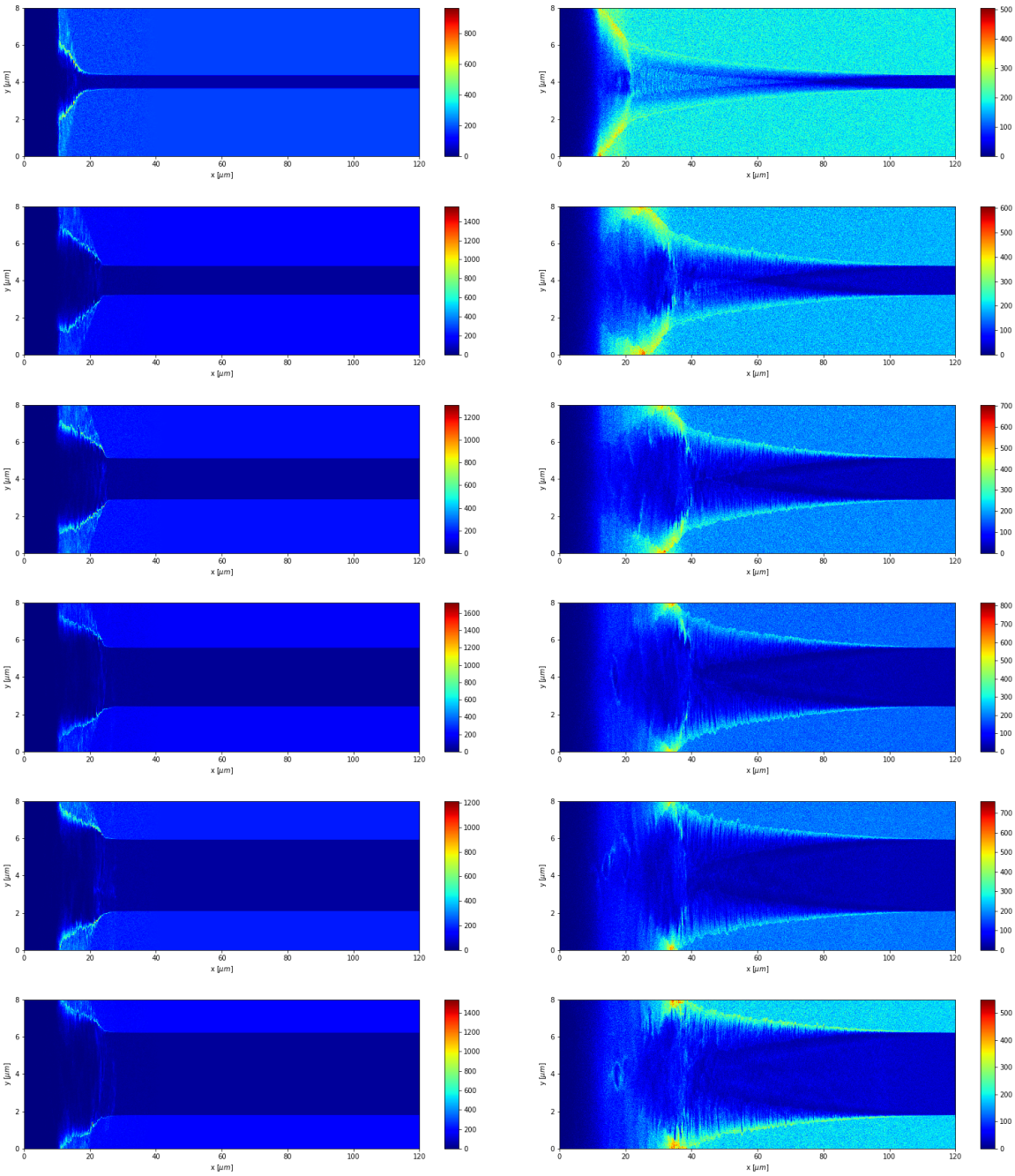

(a) $t \approx 1230\,\mathrm{fs}$ (b) $t \approx 1500\,\mathrm{fs}$

Figure 8: Channel electron densities in units of n_{cr} for simulations of a $\tau \approx 40\,\mathrm{fs}$ laser pulse with normalised amplitude $a_0 = 350$ and incident power $P_L = 1$, 5, 10, 20, 30 and 40 PW (top to bottom) comparison for times a) $t \approx 1230\,\mathrm{fs}$ and b) $t \approx 1500\,\mathrm{fs}$

$a_0 = 190$ to $a_0 = 350$ is the evolution of the channel width, as seen in Fig. 8. This is due to the higher intensity of the laser pulse for a given spot-size at higher a_0. To achieve the same amount of incident power P_L a much smaller laser spot size and therefor channel is needed (see Eq. (3.50)). Nevertheless we see the maximum value of electron density dropping for simultaneous figures for incident powers greater then $P_L = 20$. Similarly to the figures shown in Fig. 7, we can see in Fig. 8, how the shockfront approaches a planar shape from its actual Gaussian form at lower laser powers. Besides this we see a very similar evolution of the plasma density compared to $a_0 = 190$ case, including the plasma density filamentations induced by the current filamenation and Weibel instabilities. Not distinctly visible for $a_0 = 350$ case, are the laser filamentation, which is in accordance with our expectations, since the size of the laser filamentaion scales as $q_\perp^{-1} = (c/\sqrt{2}\omega_p)a_0$. At high $a_0 = 350$, the laser-spot size has to larger for the laser filamentaion instability to operate in the plasma channel and correspondingly the channel radius needs to be of similar size. This is clearly visible when taking a look at Section 4.3. The drop in maximum electron density is connected to laser filamentation instability will also be investigated in Section 4.3. To quantify the strengths of the created currents we plot their maxima over time for all incident powers P_L at each normalized amplitude a_0 in Fig. 9. For both normalized amplitudes a_0 the

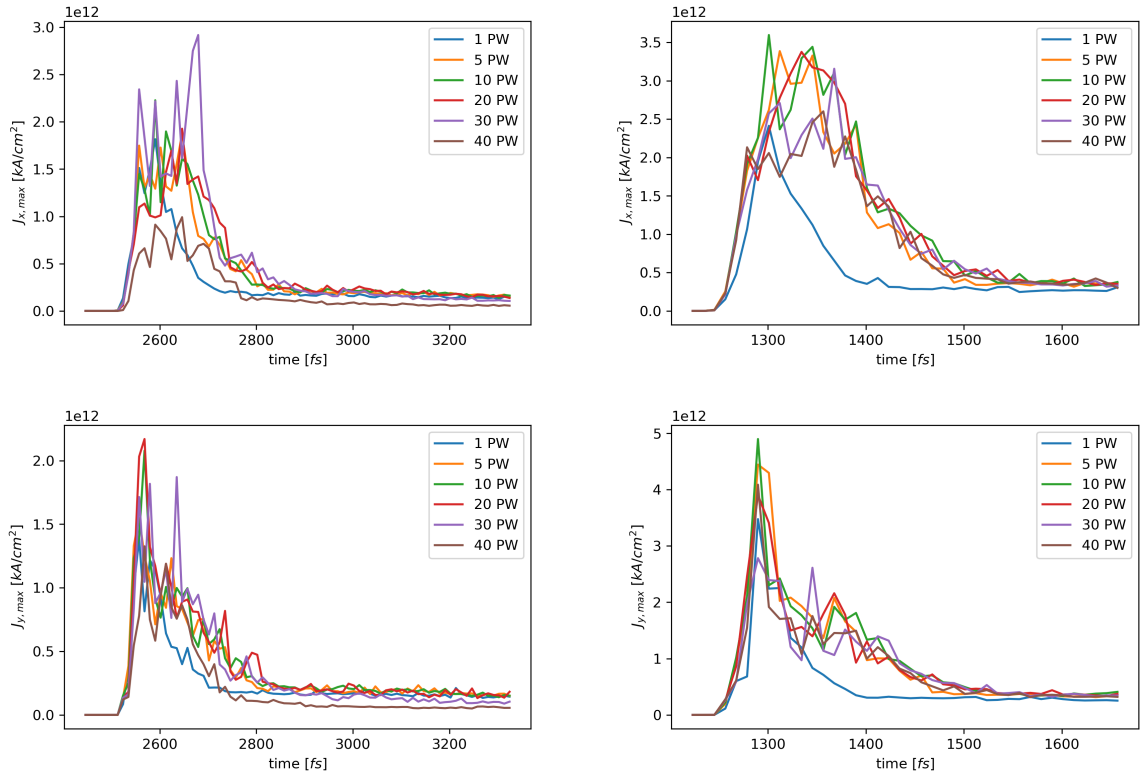

(a) $a_0 = 190$ (b) $a_0 = 350$

Figure 9: Maximum plasma current strength in [kA/cm^2] components in longitudinal (x) and transverse (y) direction (top to bottom) over time for (a) $a_0 = 190$ and (b) $a_0 = 350$.

maxima of the current components J_x and J_y reached over time are shown. The initial impact is clearly

visible on the peaks in all figures. Comparing the longitudinal current strengths (x-direction) reached for both configurations suggest a similar dynamics, however for $a_0 = 350$, the current is slightly larger in magnitude, $J_x \approx 3.5 \times 10^{12}\,\mathrm{kA/cm^2}$ then for $a_o = 190$ at $J_x \approx 3 \times 10^{12}\,\mathrm{kA/cm^2}$. Looking at the transverse current components J_y we cannot observe this relative small increase due to a more intense laser pulse. Instead the maximum current strengths are more then double as strong for $a_0 = 350$ at $J_y \approx 5 \times 10^{12}\,\mathrm{kA/cm^2}$ then for $a_0 = 190$. If we now compare each individual incident power for both normalized amplitudes we can see how the current strength reaches a maximum around $10 - 30\mathrm{PW}$ for all configurations similar to the electron density. After this the current strength drops. In the case of $a_0 = 190$ for the longitudinal currents J_x as well as for the transverse currents J_y the maximum strengths reached over time for $P_L = 40\,\mathrm{PW}$ are the lowest overall. For $a_0 = 350$ the drop in current strength is not as severe and the lowest values are reached for $P_L = 1\,\mathrm{PW}$. As we take a look at the strong current configurations we can tell that even though $P_L = 20\,\mathrm{PW}$ incident power does not strictly create the strongest currents overall respectively, they seem to be more stable at their strongest then e.g. $P_L = 10$ or $30\,\mathrm{PW}$. This is especially clear in Fig. 9 (b) when looking at J_x. Here the current maximum for $P_L = 20\,\mathrm{PW}$ does not fluctuate as much as for any other incident power P_L. This enables the plasma for $P_L = 20\,\mathrm{PW}$ at both normalized amplitudes to provide more work overall to the system. One may note that the plasma current largely depends on the plasma density employed. The onset of various instabilities can affect the plasma currents evolution significantly. The laser amplitude in this ultra-relativistic regime, has no significant effect on the plasma currents since the oscillatory velocity imparted by the laser pulse is close to the velocity of the light c in vacuum. However, the laser filamentation and hosing instabilities in a plasma channel can cause some changes in plasma currents as seen in figures before. Since at higher a_0, the same laser power can be achieved in a smaller spot-size. In these simulations, the transverse simulation window size is fixed, so the laser coupling to the plasma channel is stronger for larger spot-sizes or larger power $P_L \approx 20\,\mathrm{PW}$ at lower a_0. However, for larger a_0, the same coupling efficiency can be achieved at lower incident laser power e.g. $10\,\mathrm{PW}$ for $a_0 = 350$. Thus qualitatively, one can understand these results. For an in-depth understanding of the laser coupling, further simulations with a larger window in transverse direction are required. These simulations are computationally expansive and were not performed at the time of thesis submission.

4.2 Quasi static magnetic fields

As seen in Section 4.1, the pulse drives strong currents within the plasma channel, moving a lot of the plasma particles. These currents then create strong, slowly evolving azimuthal magnetic fields similar to a current carrying straight wire ("*Right-Hand-Rule*"). As later shown in Section 4.5 these are of strengths of up to 1% of the laser field B_0 after the initial impact ($t > 2800\,\mathrm{fs}$ for $a_0 = 190$ and $t > 1500\,\mathrm{fs}$ for $a_0 = 350$), resulting in up to $2.5\,\mathrm{MT}$ for $a_0 = 190$ and $4.5\,\mathrm{MT}$ for $a_0 = 350$, exceeding estimated field strengths $B_{z,max} \sim 10^5\mathrm{T}$ (Eq. (3.41)). These fields are visualized in Fig. 10, showing the "azimuthal" magnetic field component B_z for $a_0 = 190$ at times of $t \approx 2400$, 2600 and $3000\,\mathrm{fs}$ and for $a_0 = 350$

at times of $t \approx 1300$, 1400 and 1700 fs. Both sets of images (a) and (b) are from simulations run for incident power $P_L = 10\,\mathrm{PW}$. Looking at the earliest images we can still see the tail of the magnetic field of the incoming laser pulse up to $x = 10\,\mu\mathrm{m}$ where the plasma channel begins. From there on we can see the bell shape of the crater in which the quasi static fields begins to evolve. We can see clearly how the field is bisected by its driving current roughly along the symmetry axis of the channel, once again showing the similarity to a current carrying wire. Comparing the fields for both normalized amplitudes, the most obvious difference is the size of the field structure itself. This is most likely due to the plasma channel for $a_0 = 190$ initially being a lot wider to achieve the same incident power P_L as for $a_0 = 350$. Moving forward to the second pictures in time we can see how the static fields have grown in size but weakened in strength. Additionally one can make out the now dissolving borders of the plasma channel to the bulk plasma to the right of the primary bell like field structure, as the shockwave has traveled further trough the plasma by now. Along these borders the plasma current becomes directed again due to the bulk plasma. This creates a straight plasma current which again creates two separate azimuthal magnetic field spike-like structures around both channel borders. The current separating and driving the main static field now also shows strong hosing instability oscillations, distorting the former bell like structure. For the latest images we can see how hosing instability has broadened both field spikes along the former channel border so much, that they begin to fuse together into one field spike. This is due to the plasma currents along the former border combining into one current. The main structure of the quasi static field has further weakened and been further distorted by hosing instability. Comparing the shape

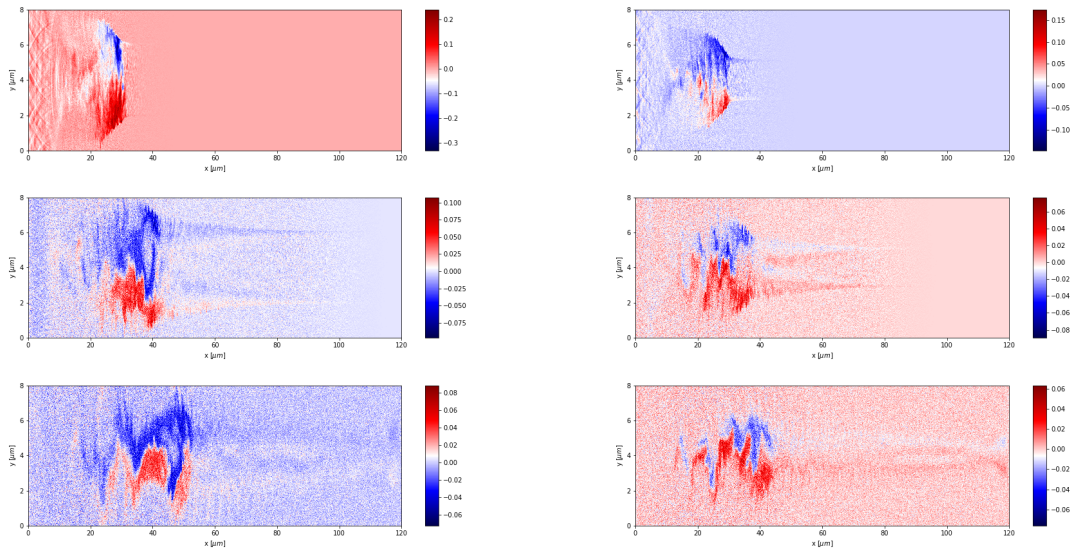

(a) $a_0 = 190$ (b) $a_0 = 350$

Figure 10: Evolution of the "azimuthal" magnetic plasma field B_z over selected timesteps at incident power of $P_L = 10\,\mathrm{PW}$ for both normalized amplitudes in units of B_0. For $a_0 = 190$ at times of $t \approx 2400$, 2600 and 3000 fs (top to bottom) and for $a_0 = 350$ at times of $t \approx 1300$, 1400 and 1700 fs (top to bottom)

of the quasi static magnetic field visible in Fig. 10 to the density maps shown previously in Section 4.1, we can tell that these strong magnetic field structures push electrons away along their gradient similar

to Eq. (2.20). This means a higher total magnetic field strength and potentially steeper gradient result in higher electron densities and stronger currents (Fig. 9). That the maximum achieved magnetic field strength has it's maximum at $P_L = 20\,\mathrm{PW}$ (compare to Fig. 23) suggests the same.

4.3 Filament size

The previously discussed drop in all major variables after an coherent maximum of $P_L = 20\,\mathrm{PW}$ seem to corroborate the theoretical suggestions discussed Section 3.3 and before. To verify this further we take a look at the filamentation instability apparent in these simulations and try to quantify their size relative to the channel and comparing it to possible predictions. For this we take a similar look into the current strength maps as we did to the density maps in Section 4.1. Visualizing the filamentation instability in a way that is visually distinct for most of the simulations was not very easy and could be further improved. Within the limitations of the thesis we will at least be able to qualitatively discuss their size. For this Fig. 11 and Fig. 12 give a good glimpse at the evolution of the filamentation instability for both applied normalized amplitudes a_0 respectively at incident power $P_L = 20\,\mathrm{PW}$. Shown are the current components along the x-direction J_x as well as the electric field component E_y, which corresponds to the laser's electric field polarization, as a map for the whole simulation window. The selected timesteps were chosen to ensure the most distinct look at the filametation. This means for earlier times the filamentation had not yet developed visually perceptible and for later times the shockfront and currents themselves slow down and weaken such, that no distinct filamentation seems to be retained and has already dissolved. In terms of their size the filaments visible in Fig. 11 show to be approximately $1 - 2\mu\mathrm{m}$ long (x-direction), visible especially in (b). In the dedicated electric field maps of E_y we can also see how the currents driven by the filamentation alter the electric field in front (to the right) of the shockfront. Behind the shockfront (left) we can see strong electric fields similar to the quasi static magnetic fields described in Section 4.2. Additionally these fields show us that in front of the shockfront is no counter-moving flow of plasma that would rule out these filaments to be due to the aforementioned Weibel instability. Thus, the filaments seen in the laser field E_y are due to the laser filamentation instability. Similarly to Fig. 11 we can see in Fig. 12, how the filaments begin to develop after the initial impact equal to the quasi static fields. The total filament size seems to be significantly larger than for $a_0 = 190$. There is a single distinct filament visible in Fig. 12 (b) developing at the center of the shockfront at a width of $0.5 - 1\mu\mathrm{m}$ and a length of $5\,\mu\mathrm{m}$. This reassures our expression for the filament size $q_\perp^- 1 \propto a_0$ as the size of the filaments roughly doubles as the normalized amplitude a_0 does as well. To understand the behaviour of the filamentation instability over the different incident powers P_L simulated a comparison of current maps of J_x for both normalized amplitudes a_0 respectively is shown in Fig. 13. Looking at the figures the most important conclusion is, that for incident powers $P_L < 20\,\mathrm{PW}$ filamentation is visually non- or nearly non-existent. This is especially the case for $a_0 = 350$, as the channel radius is around an order of magnitude smaller then the predicted filament size $q_\perp^- 1$ and as such will most likely show no visual filamentation. For further increasing incident powers the visual size of the filaments increases as

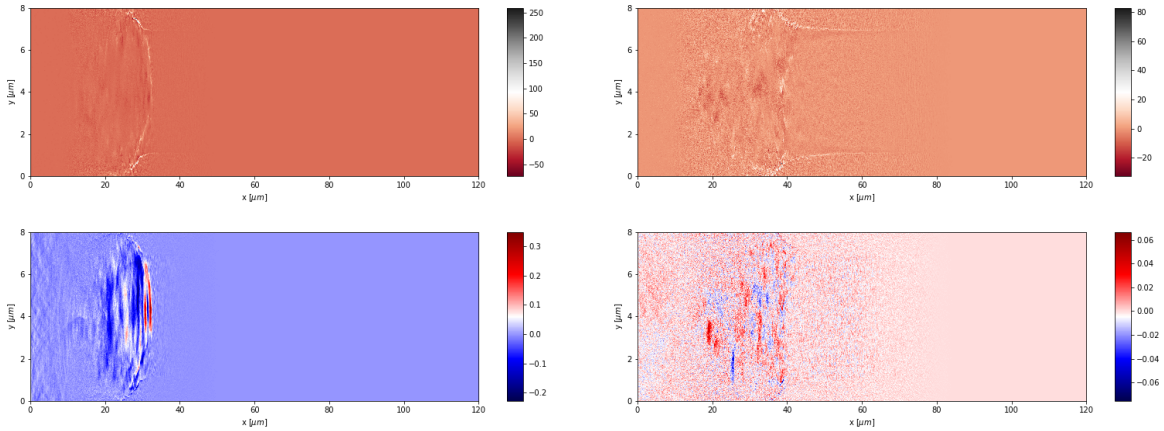

(a) $t \approx 2400\,\mathrm{fs}$ (b) $t \approx 2500\,\mathrm{fs}$

Figure 11: Plasma current component J_x in $[\mathrm{kA/cm^2}]$ and electric field component E_y in units of E_0, for given times of a plasma channel being hit with a $a_0 = 190$, $\tau \approx 40\,\mathrm{fs}$ laser pulse with incident power $P_L = 20\,\mathrm{PW}$.

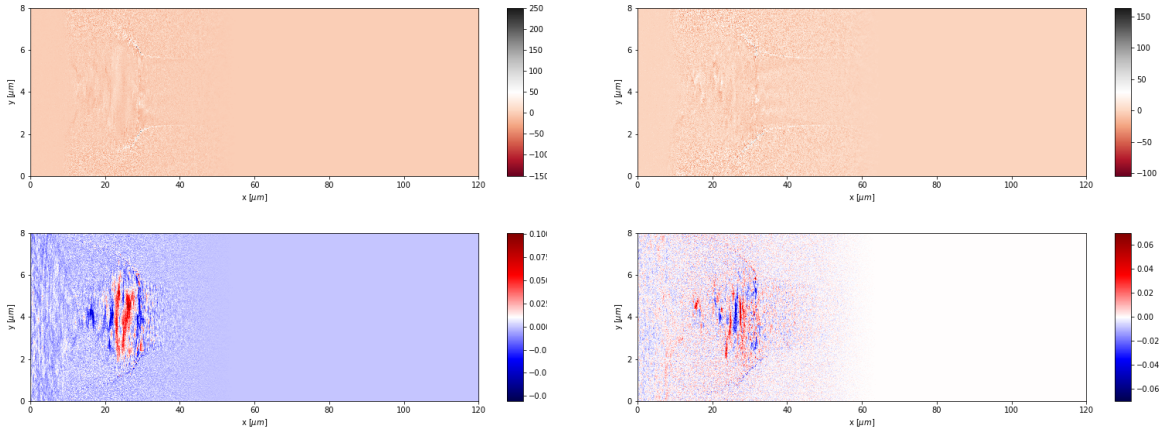

(a) $t \approx 1270\,\mathrm{fs}$ (b) $t \approx 1300\,\mathrm{fs}$

Figure 12: Plasma current component J_x in $[\mathrm{kA/cm^2}]$ and electric field component E_y in units of E_0, for given times of a plasma channel being hit with a $a_0 = 350$, $\tau \approx 40\,\mathrm{fs}$ laser pulse with incident power $P_L = 20\,\mathrm{PW}$.

the channel size does as well. Although the filaments for $a_0 = 350$ are greater in size they are fewer in number then for $a_0 = 190$. In summary filamentation instabilities occur for incident powers P_L equal or greater 20 PW for both used normalized amplitudes but are predominantly more numerous and developed at lower normalized amplitudes. This comes as their size is proportional to the normalized amplitude $q_\perp^-1 \propto a_0$. For $a_0 = 190$ the expected filament size is in the same order of magnitude as the channel width, possibly enhancing or rather enabling their growth, compared to the the expected filament size $q_\perp^-1$ being an order of magnitude larger than the channel width for $a_0 = 350$, possibly preventing distinct filamentation growth.

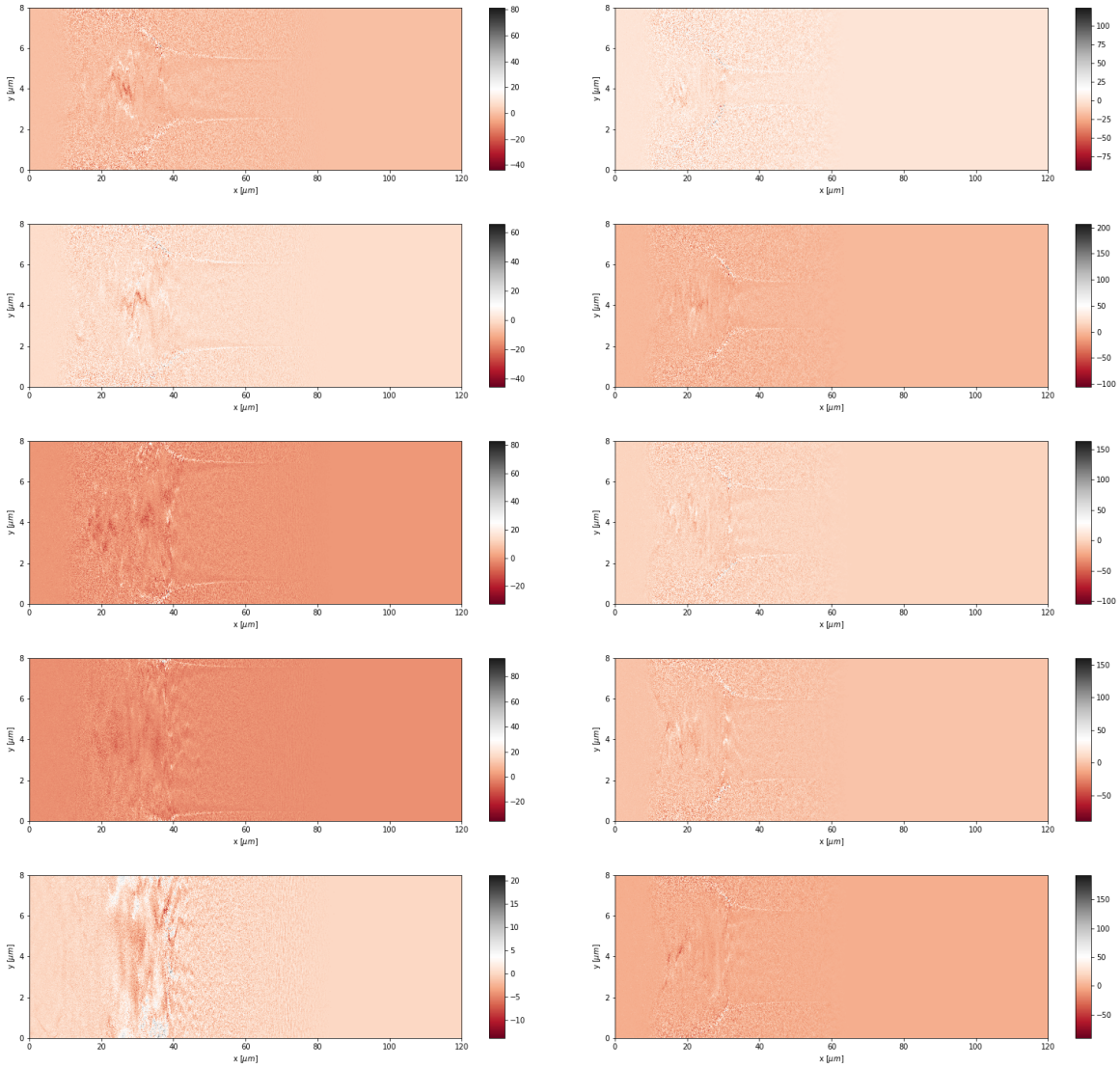

(a) $a_0 = 190$ $t \approx 2500\,\mathrm{fs}$ (b) $a_0 = 350$ $t \approx 1300\,\mathrm{fs}$

Figure 13: Plasma current component J_x in [kA/cm^2] for simulations of a $\tau \approx 40\,\mathrm{fs}$ laser pulse with normalised amplitude (a) $a_0 = 190$ and (b) $a_0 = 350$ for incident power $P_L = 5$, 10, 20, 30 and 40 PW (top to bottom) compared at given times.

4.4 Emission behavior

To examine the emission behaviour of the plasma in more detail and see if the previous pattern translates into it we take a look at the Synchrotron emission power parameter η (Eq. (2.24)). To understand the temporal evolution as well as the highest values reached over time, we take a look at Fig. 14. Again we focus on the initial impact which is clearly visible for both sets of simulations and contains the bulk of radiation generation. Emissions generally peak at values around an above $\eta \approx 5$ for $a_0 = 190$. For all incident powers P_L the maximum values for η are close to each other except for $P_L = 30\,\mathrm{PW}$, which marks the overall maximum for $a_0 = 190$ at $\eta \approx 9$. For a further increase of P_L to 40 PW maximum emission power drops to a similar level as for $P_L = 5 - 10\mathrm{PW}$. Another prominent feature is the quick drop after

the initial impact of the laser pulse for $P_L = 1\,\mathrm{PW}$ around $t \approx 2570\,\mathrm{fs}$. As for higher configurations of P_L the emission of high power synchrotron radiation ($\eta \gtrsim 1$) is upheld for a duration of roughly 200 fs after the initial impact. However for $P_L = 1\,\mathrm{PW}$ it drops below this mark after just around $30 - 50\mathrm{fs}$. In the case of $a_0 = 350$ we see a more distinct scaling with incident power P_L as well as a global increase in emission power with η values up to $\eta \approx 70$, about ten times higher then for $a_0 = 190$. For $P_L = 1\,\mathrm{PW}$ emission power shows comparably low levels with a maximum around $\eta \approx 5$. Additionally, over time the evolution of emission power shows a similar behaviour for $P_L = 1\,\mathrm{PW}$ when comparing to the simulations done for $a_0 = 190$, as it does not sustain high power emissions as long as simulations of higher incident powers do, just around 50 fs. On the contrary for all simulations with $P_L > 1\,\mathrm{PW}$ we observe nearly the same drop-off of emission power over a duration of more then 100 fs after emissions for $P_L = 1\,\mathrm{PW}$ have already dropped to $\eta \approx 0$. The overall maximum is reached for $P_L = 10\,\mathrm{PW}$ around $\eta \approx 70$ after which values drop for increasing incident power P_L, although not strictly. This means that for both $P_L = 20\,\mathrm{PW}$ and 30 PW as well as higher incident powers, the maximum snychrotron emission power lies below that of $P_L = 10\,\mathrm{PW}$. However $P_L = 30\,\mathrm{PW}$ shows higher emission powers then 20 PW. The same pattern is observed for $a_0 = 190$, although $P_L = 30\,\mathrm{PW}$ does achieve higher power emission then 10 PW instead as discussed before. As we discussed the highest emissions occurring over time we want to understand

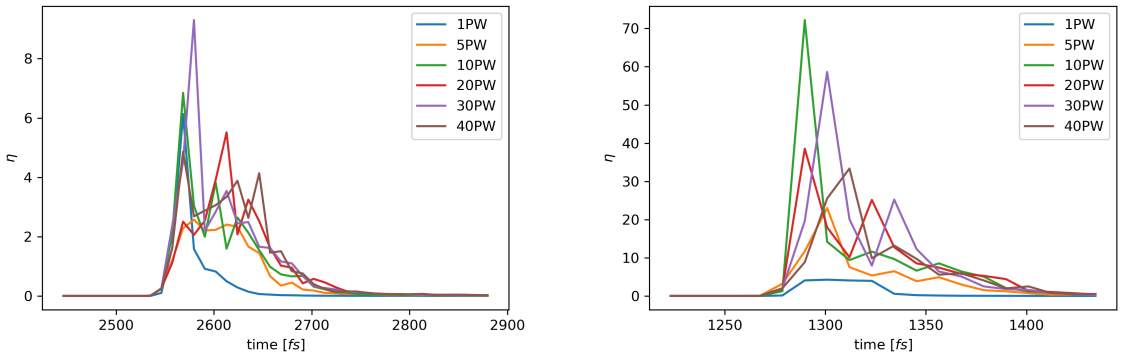

(a) $a_0 = 190$ (b) $a_0 = 350$

Figure 14: Maximum synchrotron emission power variable η over time for all indicated incident powers P_L at normalized laser amplitudes a) $a_0 = 190$ and b) $a_0 = 350$.

more about the spatial distribution of emissions and their evolution over time. For this, η was plotted along the symmetry axis of the laser channel at $y = 4\,\mu\mathrm{m}$ in Fig. 15 and Fig. 16. This was chosen to give a balanced representation of all emissions, even though the area of highest emissions is expected to be at the inner channel borders, e.g. at $y = 4\,\mu\mathrm{m} \pm R$. It should also be noted, that Fig. 15 and Fig. 16 have the time axis given in timesteps $\Delta t \approx 0.002\,\mathrm{fs}$. Since only values $\eta \leq 0.005 = \eta_{max}$ are plotted to ensure a better visual representation, the highest emissions cannot be identified but will be displayed as η_{max} emissions. Since these figures are meant to discuss the spatial evolution of emissions this is neglectable especially since the maximum values for η over time have already been discussed before and been shown in Fig. 14. Nonetheless it is clearly visible that for all simulations the initial impact of the laser pulse into

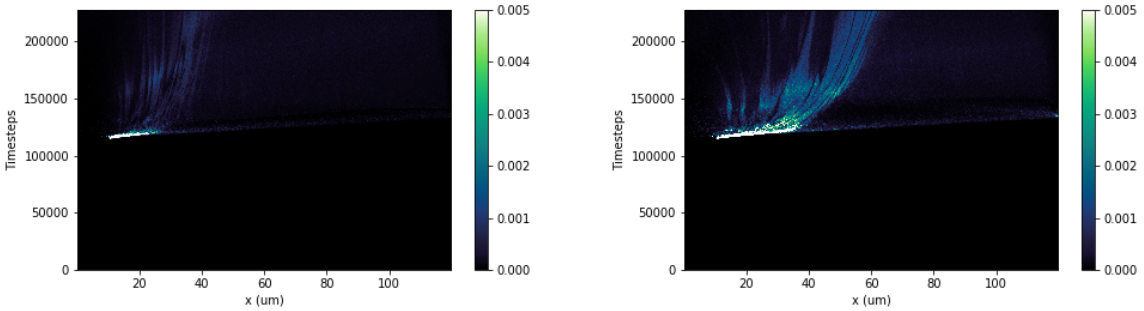

(a) $P_L = 1\,\mathrm{PW}$ (b) $P_L = 5\,\mathrm{PW}$

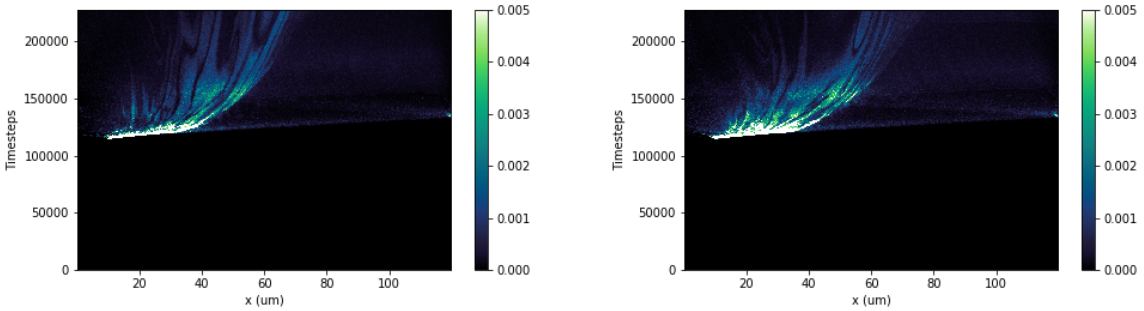

(c) $P_L = 10\,\mathrm{PW}$ (d) $P_L = 20\,\mathrm{PW}$

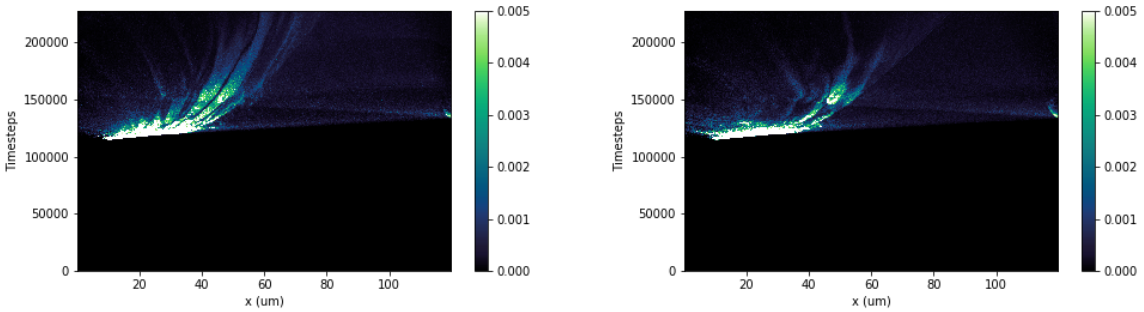

(e) $P_L = 30\,\mathrm{PW}$ (f) $P_L = 40\,\mathrm{PW}$

Figure 15: Synchrotron emission parameter η plotted along the symmetry axis ($y = 4\,\mu\mathrm{m}$) of the plasma channel over time for simulations of a $\tau \approx 40\,\mathrm{fs}$ laser pulse with incident Power $P_L = 1$, 5, 10, 20, 30 and 40PW comparison for normalised amplitude $a_0 = 190$. The colorbar indicates the Synchrotron emission power parameter η (Eq. (2.24)) and is limited to values up to $\eta = 0.005$ (higher values are depicted as $\eta = 0.005$) to enhance visibility.

the plasma channel itself creates a high amount of these η_{max} photons. These emissions are visible at the beginning of the first diagonal line which is visible for all incident powers. This represents the initial shockwave of the laser pulse hitting the plasma channel, going along the full length of the channel in the x-direction over a short period of time ($\sim 5000\Delta t \approx 10\,\mathrm{fs}$). The highest emissions of the initial impact seem to happen up to a depth of around $30\,\mu\mathrm{m}$ ($x = 40\,\mu\mathrm{m}$) for all simulations. After this depth there is still photon production, however not as energetic, $\eta \lesssim 0.002$ for $a_0 = 190$ and $\eta \lesssim 0.003$ for $a_0 = 350$. Once the shockwave reaches the end of the channel it gets reflected on the boundary layer of the plasma to the empty simulation space. This is especially apparent in Fig. 15 (d), (e) and (f) or Fig. 16 (f). We

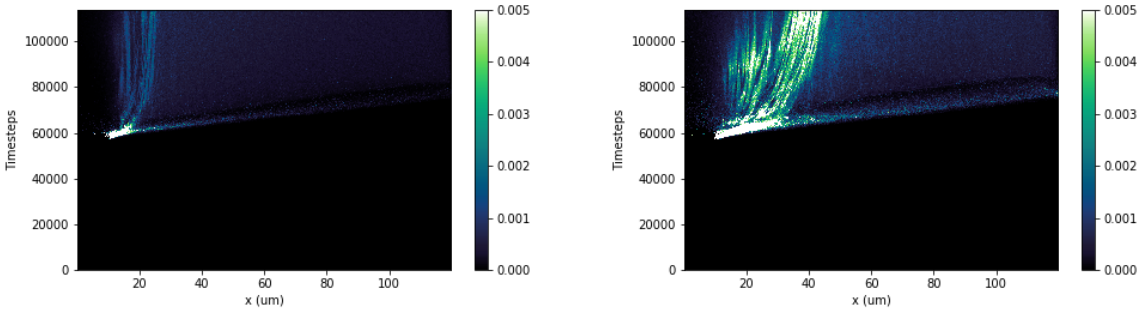

(a) $P_L = 1\,\mathrm{PW}$ (b) $P_L = 5\,\mathrm{PW}$

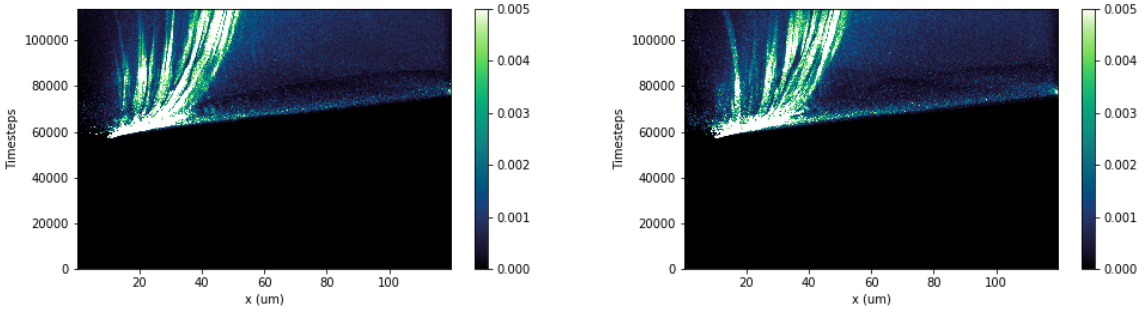

(c) $P_L = 10\,\mathrm{PW}$ (d) $P_L = 20\,\mathrm{PW}$

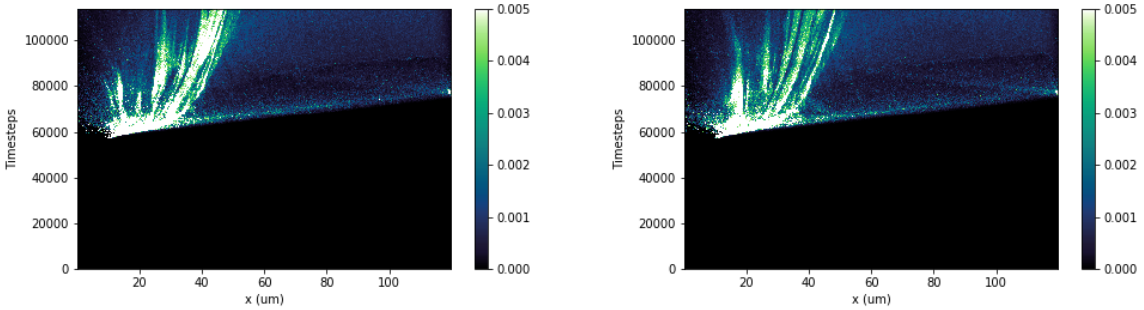

(e) $P_L = 30\,\mathrm{PW}$ (f) $P_L = 40\,\mathrm{PW}$

Figure 16: Synchrotron emission parameter η plotted along the symmetry axis ($y = 4\,\mu\mathrm{m}$) of the plasma channel over time for simulations of a $\tau \approx 40\,\mathrm{fs}$ laser pulse with incident Power $P_L = 1$, 5, 10, 20, 30 and 40PW comparison for normalised amplitude $a_0 = 350$. The colorbar indicates the Synchrotron emission power parameter η (Eq. (2.24)) and is limited to values up to $\eta = 0.005$ (higher values are depicted as $\eta = 0.005$) to enhance visibility.

can see this reflection as a second diagonal line going from the end point of the first one on the right hand end of the figures, tilted in the opposite direction as the diagonal line of the first shockwave. However over time there occur more high η Synchrotron emission. These are visible as arcs stretching up from the emission bulge of the initial impacts. Comparing this behaviour to the quasi static magnetic fields created by the strong plasma currents described in Section 4.2 we can assume that these emissions are caused by the slowly evolving quasi static fields. Additionally as the reflected shockwave impinges these quasi static fields emissions parameters are enhanced which is especially visible in Fig. 15 (e) and (f). The same structures are visible for $a_0 = 350$ in Fig. 16. To qualitatively check this assumption selected

maps of the magnetic fields B_z as well as the corresponding maps of electron density overlayed by η for each emission at that time with values $\eta \gtrsim 0.0004$ at incident power $P_L = 1\,\mathrm{PW}$ in Fig. 17 and Fig. 18. This shows undoubtedly the direct correlation between the magnetic field strength and the synchrotron emission power $P_{synch} \propto \eta$. As the fields increase in strength the emission power is enhanced while an increase in field size increases the total number of emissions.

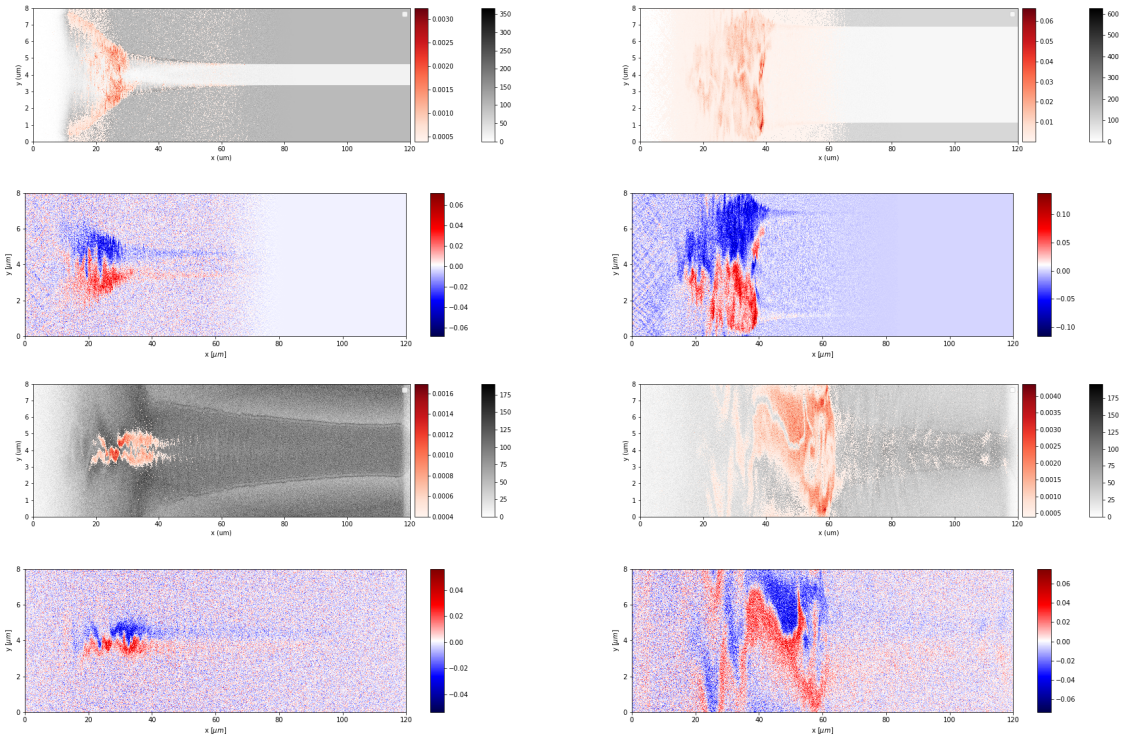

(a) $P_L = 1\,\mathrm{PW}$ (b) $P_L = 20\,\mathrm{PW}$

Figure 17: Electron density n_e (greyscale colorbar) overlayed with η for emission events $\eta \geq 0.0004$ (redscale colorbar) and corresponding "azimuthal" magnetic field B_z in units of B_0 for the simulation of a laser pulse with normalized amplitude of $a_0 = 190$ for selected incident powers P_L at $t \approx 2500\,\mathrm{fs}$ (top) and $t \approx 3400\,\mathrm{fs}$ (bottom)

4.5 MeV Photon generation scaling the laser power P_L

To quantify the emission behaviour it is necessary to first look at the global parameters of the simulation. To begin with we want to examine the total energy contained in the simulation window. For both $a_0 = 190$ and $a_0 = 350$ we can see, that the pulse enters the simulation window around half of the simulation time T_{sim}. Since the channel's electrons as well as the ions were initially at rest the energy peak $U_{tot,max}$ corresponds to the pulse's total energy ($U_{tot,max} = E_{Laser}$). This energy becomes primarily converted into kinetic energy of the plasma's particles, which then are able to emit high energy photons as synchrotron radiation. Over time the total amount of energy drops due to accelerated particles and radiation leaving the simulation window. To compare the amount of photons generated we look at Fig. 20. Here the normalized number of photons $\tilde{N}_\gamma = N_\gamma 1\,\mathrm{PW}/P_L[PW]$ at that point in time within

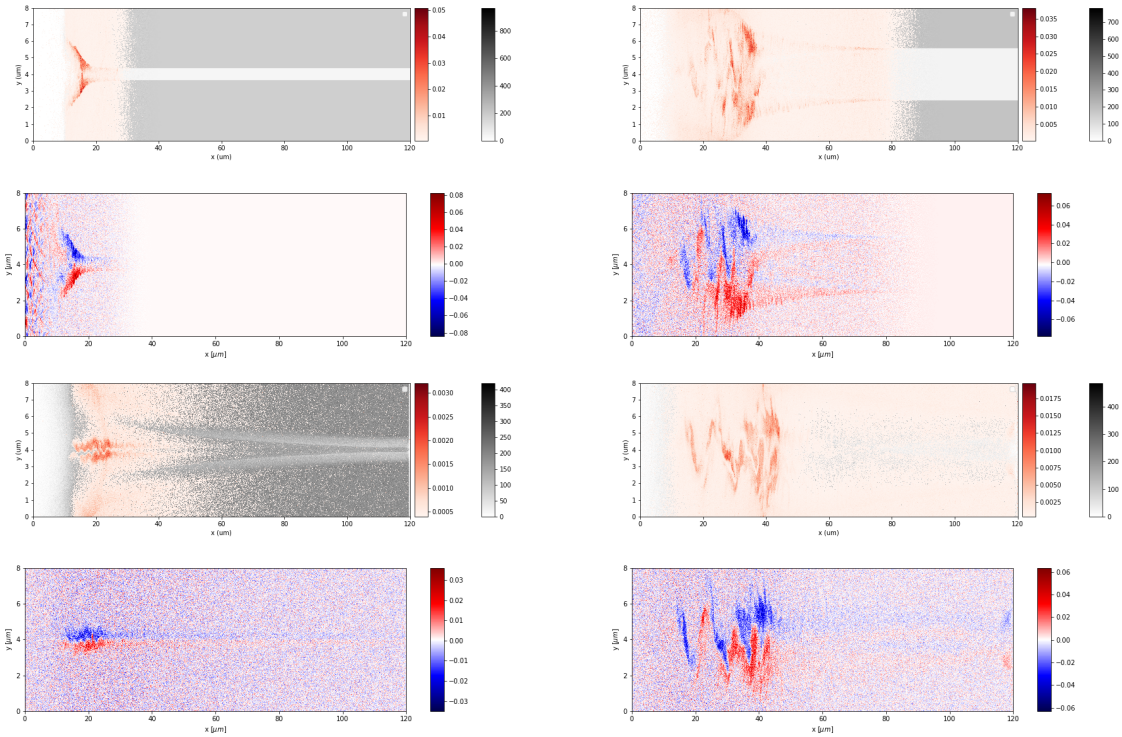

(a) $P_L = 1\,\mathrm{PW}$ (b) $P_L = 20\,\mathrm{PW}$

Figure 18: Electron density n_e (greyscale colorbar) overlayed with η for emission events $\eta \geq 0.0004$ (redscale colorbar) and corresponding "azimuthal" magnetic field B_z in units of B_0 for the simulation of a laser pulse with normalized amplitude of $a_0 = 350$ for selected incident powers P_L at $t \approx 1230\,\mathrm{fs}$ for $P_L = 1\,\mathrm{PW}$ and $t \approx 1400\,\mathrm{fs}$ for $P_L = 20\,\mathrm{PW}$ (top) and $t \approx 1700\,\mathrm{fs}$ (bottom)

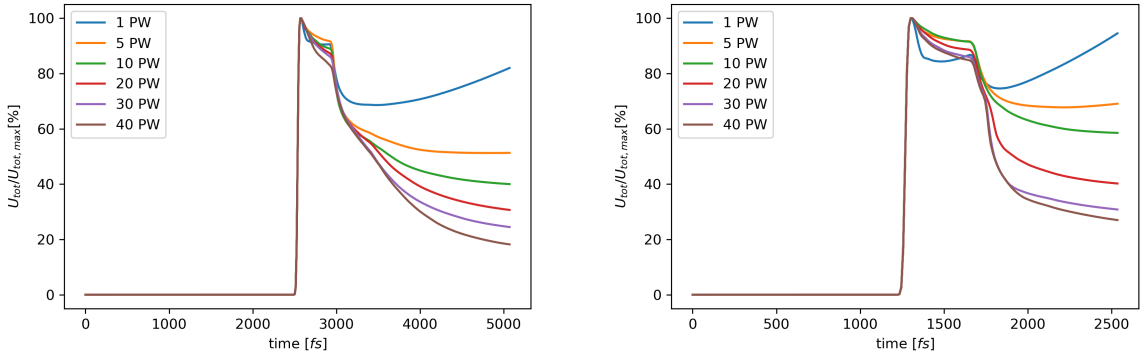

(a) $a_0 = 190$ (b) $a_0 = 350$

Figure 19: Total energy contained in simulation window normalized to the maximum value reached in each simulation respectively

the the simulation window is shown. The gradual decrease in photon number at later times is due to the finite duration of the laser pulse. The photon generation is expected to be ceased after a while since the laser pulse has a finite duration and it constantly imparts energy to plasma particles and MeV photons. Similar to the progression of $U_{tot,max}$ we can see the initial spike of the pulse's impact around $T_{sim}/2$

after which photon numbers lower slowly until it drops drastically around $t \approx 3000\,\text{fs}$ for $a_0 = 190$ and around $t \approx 1700\,\text{fs}$. Besides the total number of photons in general all simulation setups show the same progression. Especially the power scaling with P_L for each normalized amplitude a_0 is identical for both setups. Up until $P_L = 10\,\text{PW}$ $\tilde{N}_\gamma$ increases to its maximum. For further increasing incident power P_L the normalized photon number drops even further, suggesting a decrease in total photon emission. The power spectrum of the resulting radiation is given in Fig. 21 for all simulations. It is clearly

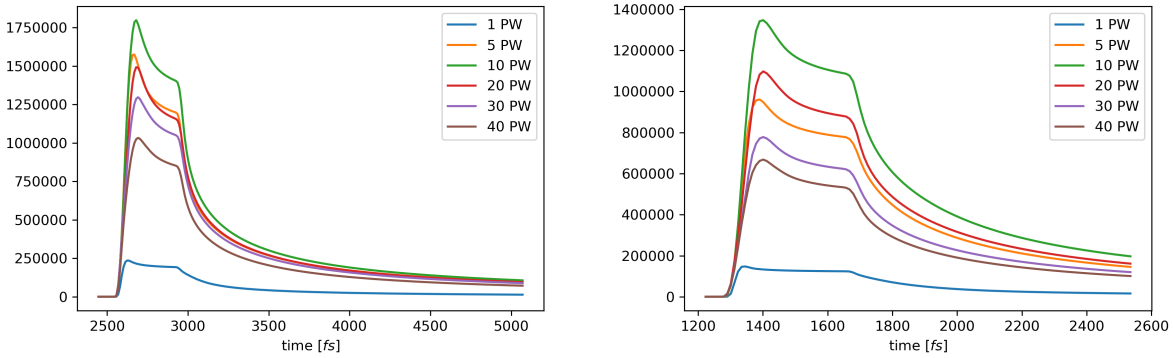

(a) $a_0 = 190$ (b) $a_0 = 350$

Figure 20: Normalized number of photons $\tilde{N}_\gamma = N_\gamma 1\,\text{PW}/P_L[PW]$ within the simulation window over time for normalized laser amplitude a) $a_0 = 190$ and b) $a_0 = 350$.

visible how the laser intensity, e.g. its normalized amplitude a_0 affects the maximum emission power as the maximum sampled photon energy for $a_0 = 190$ lies around 180 MeV and for $a_0 = 350$ at around 320 MeV. Additionally the number of photons sampled per MeV is up to one order of magnitude higher for each emission spectrum at $a_0 = 350$ than for $a_0 = 190$. Generally both sets of spectra show similar power scaling with P_L. As one would expect an increase in incident power P_L results in higher overall number of photons and a higher maximum photon energy. However this seems not to be the case for incident powers $P_L \geq 20\,\text{PW}$, as the spectra for 20, 30 and 40 PW are nearly the same, with the highest maximum photon energy sampled for $P_L = 20\,\text{PW}$. This suggests that total emissions saturate at these incident powers for $a_0 = 350$. Moreover the power spectrum seems to be in some way proportional to the normalized laser amplitude a_0 as maximum photon energies and the number of photons sampled for their respective energy roughly doubles as does a_0 going from 190 to 350. This would suggest saturation of emission for $a_0 = 190$ at around $P_L = 40\,\text{PW}$, which is supported by the spectra in Fig. 21 (a). Here the maximum photon energy is sampled for $P_L = 30\,\text{PW}$ although for $P_L = 40\,\text{PW}$ photon numbers are slightly higher for energies exceeding 100 MeV. In Fig. 22 the total energy conversion efficiencies ϵ (Eq. (3.42)) are plotted for all simulations to compare from $t = \frac{1}{2}T_{sim}$ on, since we can tell from Fig. 19, that the pulse does not enter the simulation window before. We find, that with increasing incident power P_L the efficiency increases as expected. However this relative increase does not seem to be trivially linear. For example for $a_0 = 190$ in Fig. 22 (a) we can see that the five-fold increase in incident power $P_L = 1 \to 5$ PW does correspond to a great relative efficiency increase from $\epsilon \approx 1.2\%$ to roughly

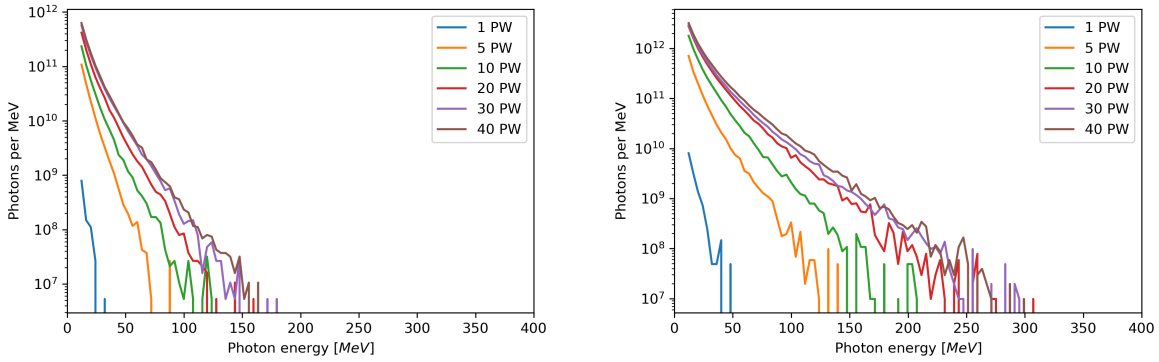

(a) $a_0 = 190$ (b) $a_0 = 350$

Figure 21: Radiation Spectrum in MeV and MeV^{-1} for all incident powers P_L = 1, 5 ,10, 20, 30 and 40 PW at a) $a_0 = 190$ and b) $a_0 = 350$.

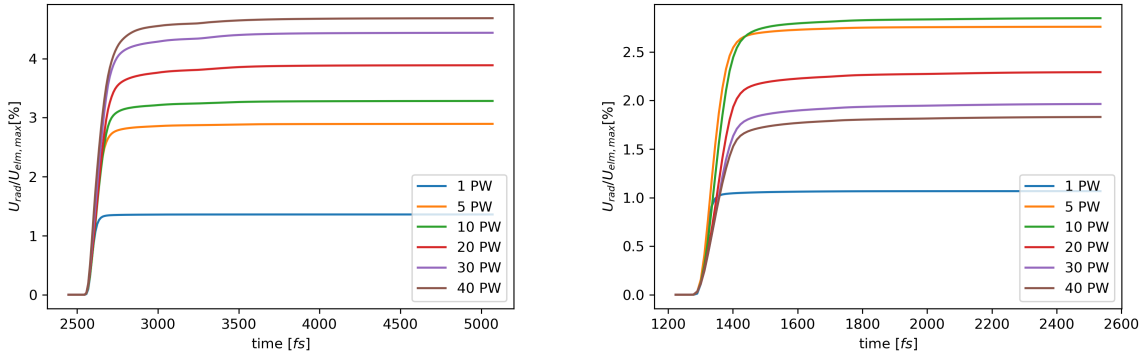

(a) $a_0 = 190$ (b) $a_0 = 350$

Figure 22: Conversion efficiency of laser energy into radiation in percentages of the maximum total energy $U_{tot,max}$ of the system

2.8% of $\Delta\epsilon \approx 1.6\%$. Once the incident power gets doubled from $P_L = 5\,\text{PW}$ to 10 PW and then 20 PW, the relative efficiency increase also approximately doubles from $\Delta\epsilon_{5\to10} \approx 0.3\%$ to $\Delta\epsilon_{10\to20} \approx 0.6\%$. Contradicting this pattern doesn't seem to hold up for increasing incident powers P_L as the relative efficiency increase stays approximately constant $\Delta\epsilon_{20\to30} \approx 0.6\%$. Nevertheless this result should be taken with care since for these simulations the channel's bulk is very small and for $P_L = 40\,\text{PW}$ not even present in the simulation box (see Section 4.1). Comparing this to the results for $a_0 = 350$ in Fig. 22 (b) we see a strongly different behaviour. For $P_L = 1\,\text{PW}$ as well as 5 PW we see nearly the same efficiency as at $a_0 = 190$, with $\epsilon_1 \approx 1.0\%$ and $\epsilon_5 \approx 2.7\%$. However for $P_L = 10\,\text{PW}$ we see that it is just slightly more efficient in terms of global energy conversion than at $P_L = 5\,\text{PW}$ with $\epsilon_{10} \gtrsim \epsilon_5$. For further increasing incident power P_L the efficiency drops again. However we can see that this drop scales roughly with ΔP_L as $\Delta\epsilon_{10\to20} \gtrsim \Delta\epsilon_{20\to40}$, $\Delta\epsilon_{10\to20} \approx \frac{1}{2}\Delta\epsilon_{20\to30}$ and $\Delta\epsilon_{10\to20} \approx \frac{1}{3}\Delta\epsilon_{30\to40}$. Comparing this drop in efficiency to the power spectra shown in Fig. 21 (b) comes as now surprise, since with increasing incident power more energy is put into the system in total by the laser but emissions saturate for $P_L \geq 20\,\text{PW}$

resulting in a drop in conversion efficiency ϵ. If we now take a look at the maximum electromagnetic field strengths in Fig. 23, we can already tell how the radiation power P_{synch} (Eq. (2.24)) and therefor the emission efficiency ϵ relates to these. Especially visible is the relative increase from $B_{z,max}/B_0 \approx 0.7$

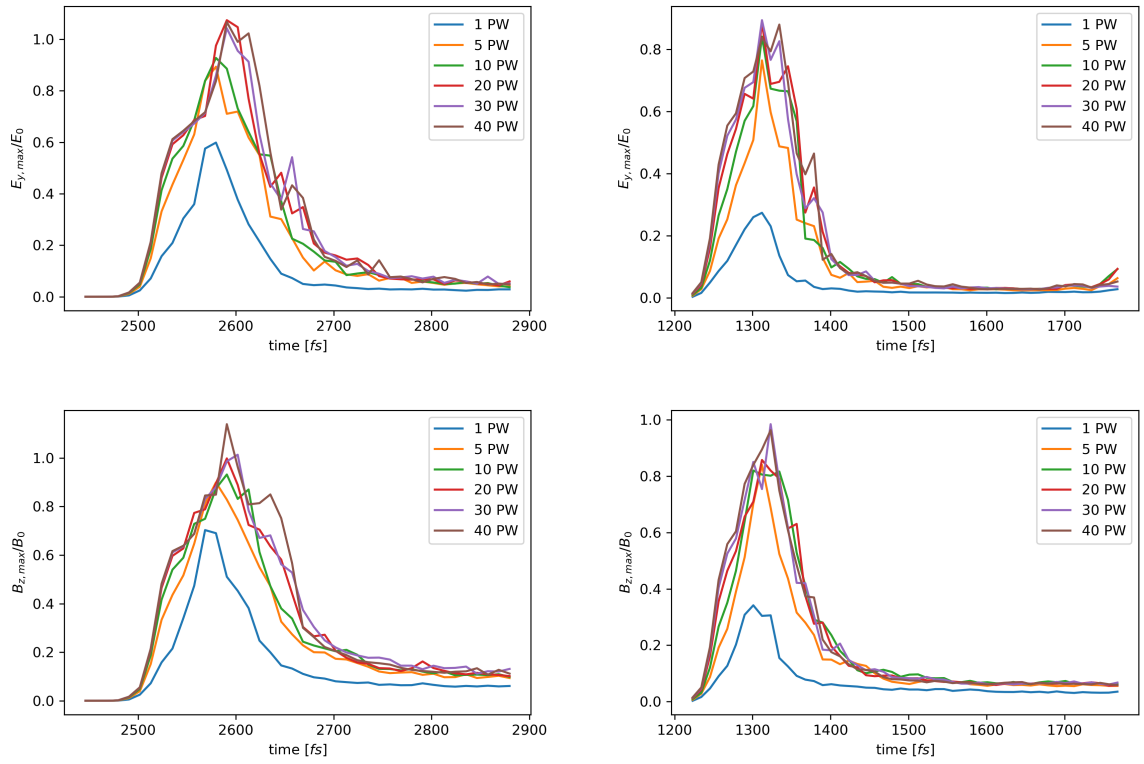

(a) $a_0 = 190$ (b) $a_0 = 350$

Figure 23: Maximum magnetic field strength component along the y-axis and maximum magnetic field strength component along the z-axis, corresponding to the azimuthal component in 3D cylindrical coordinates, over time. Normalized each to the laser pulse's electric field strength E_0 (Eq. (2.16)) and B_0 (Eq. (2.17))

to 0.9 for the increase of $P_L = 1\,\mathrm{PW}$ to $5\,\mathrm{PW}$, after which for further increasing P_L the maximum field strength just barely increases. This is particularly visible when looking at the electric field strengths, which seems to saturate for $P_L > 20\,\mathrm{PW}$ at around $E_{y,max}/E_0 \approx 1.1$. This strong increase in both electric and magnetic field strength when going from $P_L = 1\,\mathrm{PW}$ to $5\,\mathrm{PW}$ indicates a correspondence to the aforementioned great relative increase in efficiency $\Delta\epsilon_{1\to5}$. In addition to that the saturated field strengths indicate, that the efficiency should be proportional to the incident power P_L, as suggested by $\Delta\epsilon_{5\to10}$ and $\Delta\epsilon_{10\to20}$. Comparing this to the results to the ones $a_0 = 350$ we can see that first and foremost the pulse hits the plasma channel almost half as quick. This is the reason why the simulation itself was carried out for only half the time, e.g. $T_{sim,190} = 2 \times T_{sim,350}$. For the total energy in the simulation window U_{tot}, shown in Fig. 19 (b) we can see, that the evolution is otherwise similar although faster. Taking a look at the conversion efficiency ϵ in Eq. (3.42) (b) we can see, that for an incident power of $P_L = 20\,\mathrm{PW}$ the efficiency reaches a maximum and drops afterwards with rising incident power. Since

$\epsilon_{5\,\mathrm{PW}} \lesssim \epsilon_{10\,\mathrm{PW}}$, we can assume that for $a_0 = 350$ the conversion efficiency saturates around $P_L = 10\,\mathrm{PW}$ and begins to drop due to other effects for higher values of P_L. This corresponds to the maximum of relative photon production $\tilde{N}_\gamma$ (Fig. 20) as well. It should be noted, that these values for the conversion efficiency ϵ are for total photon generation and not specifically directed high energy multi-MeV photons. This will be discussed in Section 4.6. Furthermore when comparing Fig. 23 (a) to (b), we can see that for $a_0 = 350$ the electric and magnetic field strengths achieved are in general about $0.2/E_0$ or $0.2/B_0$ weaker then for $a_0 = 190$. On top of this the strength of the fields created for incident power $P_L = 1\,\mathrm{PW}$ is considerably lower relative to higher incident powers, which for each normalized amplitudes saturate above a couple PW. To put this into numbers, for $a_0 = 190$ the maximum field strengths achieved for both electric and magnetic fields, over the simulation for $P_L = 1\,\mathrm{PW}$ are approximately half as strong as the total maximum for all incident powers. For $a_0 = 350$ however the maximum field strengths at $P_L = 1\,\mathrm{PW}$ barely reaches 30% of the total maximum for all incident powers, while the field strengths for this already go into saturation for $P_L \geq 5\,\mathrm{PW}$. After the initial impact for all simulations the magnetic field strengths are still in orders of 0.1 to 1% of the respective laser field B_0, reaching strengths of multi-MT, depicting the created quasi static magnetic fields created by the strong plasma currents as described in Section 4.2. The electric fields otherwise drop to approximately 0 after the initial impact as the laser gets absorbed. However we can see a temporal rise around 3000 fs for $a_0 = 190$ and at the end of the simulation for $a_0 = 350$. Interestingly we see here, that the maximum electric field strength $E_{y,max}$ for each normalized intensity a_0 again shows a maximum at $P_L = 20\,\mathrm{PW}$. Although not visible in Fig. 23, we know from Section 4.2 that this is equal for the magnetic field after the initial impact. Further it is visible, that the second drop in total energy as well as photon number N_γ (or $\tilde{N}_\gamma$) within the system at around $t \approx 3000\,\mathrm{fs}$ for $a_0 = 190$ and around $t \approx 1700\,\mathrm{fs}$ (Fig. 19) corresponds to the "azimuthal" magnetic field B_z dropping below the critical value $B_{z,crit}$ (Eq. (3.40)), therefor drastically decreasing synchrotron emission as well as emission power. One may note that this does not imply that that for $a_0 = 350$ the high-energy photon generation is smaller. Only the generation of low-energy photons seems to be less efficient at higher incident laser power as well as higher a_0 (see Section 4.6). The apparent generation of weaker azimuthal magnetic fields for the high a_0 case signifies the inefficiency of the electron acceleration in the plasma channel. Efficient electron acceleration in a plasma channel is required for generating and maintaining a strong quasi-static magnetic field due to various filamentation dynamics.

4.6 Brilliance of γ-photon beam and quality of emission

Since we are interested in the creation of collimated high energy γ-ray generation the efficiencies discussed in Section 4.5 are not as significant as the efficiency converting incident laser energy into these directed high energy beams. To quantify this we look into the angular distribution of the emitted photons and their energy distribution in Fig. 24 for $a_0 = 190$ and Fig. 25 for $a_0 = 350$ respectively. Due to the simulation for $a_0 = 190$ at $P_L = 40\,\mathrm{PW}$ not having bulk plasma surrounding the channel, this simulation was carried put again with an increased simulation width (x-direction) of 10 µm with identical resolution

along the x-axis to enable comparison to the other simulations. The angle Φ indicates the direction of emission in respect to the channel's symmetry axis along $y = 4\,\mu\text{m}$. Across all angular spectra we can see how the highest emission energies are collimated around $\Phi = \pm 45^{\circ}$. As a consequence of this we define the beams to be analysed as the emission cone at $\Phi = \pm 45^{\circ} \pm 10^{\circ}$. Especially looking at Fig. 25 we can see that this cone of $\pm 10^{\circ}$ includes most of the high energy multi-MeV emission we are interested in.

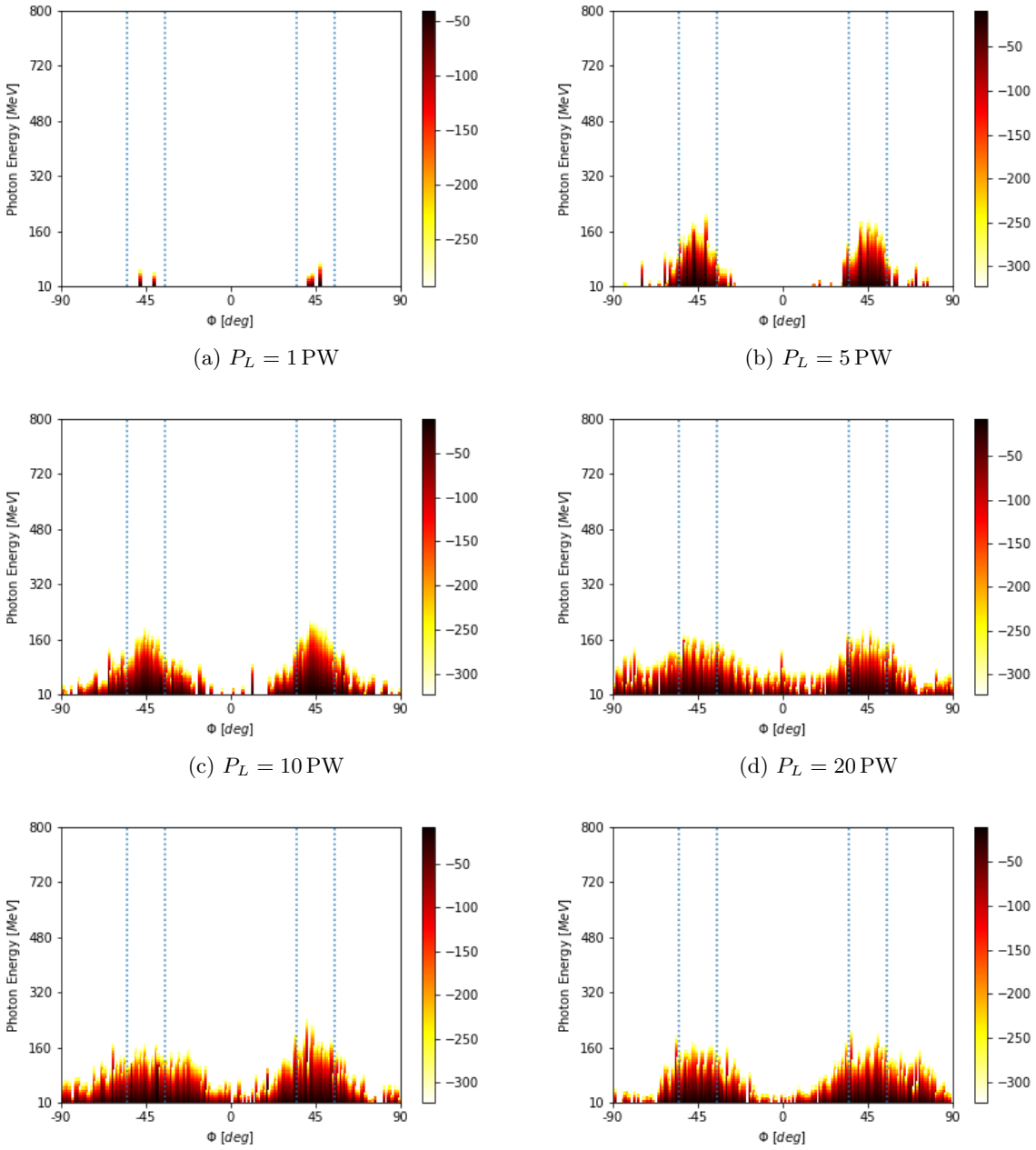

(a) $P_L = 1\,\text{PW}$ (b) $P_L = 5\,\text{PW}$

(c) $P_L = 10\,\text{PW}$ (d) $P_L = 20\,\text{PW}$

(e) $P_L = 30\,\text{PW}$ (f) $P_L = 40\,\text{PW}$

Figure 24: Angular distribution of photon energy spectrum in *degree* in respect to the channel' symmetric axis and MeV for $a_0 = 190$ at incident powers $P_L = 1$, 5, 10, 20, 30 and 40PW ((a) to (f)) compared as an average of total simulation time. The colorbar gives the number density in units of $log(n_{cr})$ and the dotted blue line indicates the beams defined as the emission cone at $\Phi = \pm 45^{\circ} \pm 10^{\circ}$.

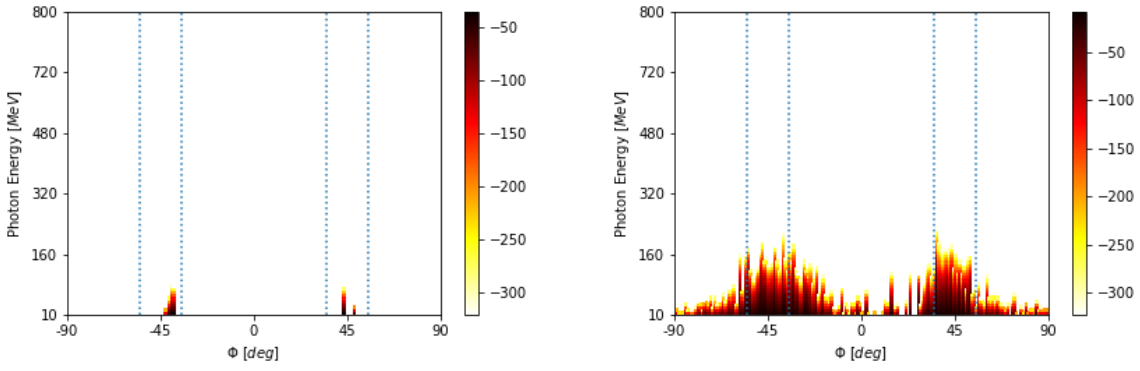

(a) $P_L = 1\,\mathrm{PW}$ (b) $P_L = 5\,\mathrm{PW}$

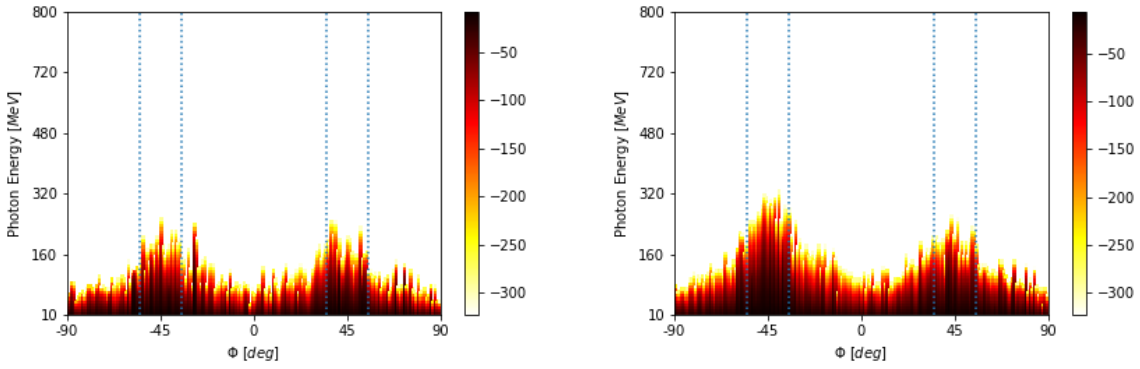

(c) $P_L = 10\,\mathrm{PW}$ (d) $P_L = 20\,\mathrm{PW}$

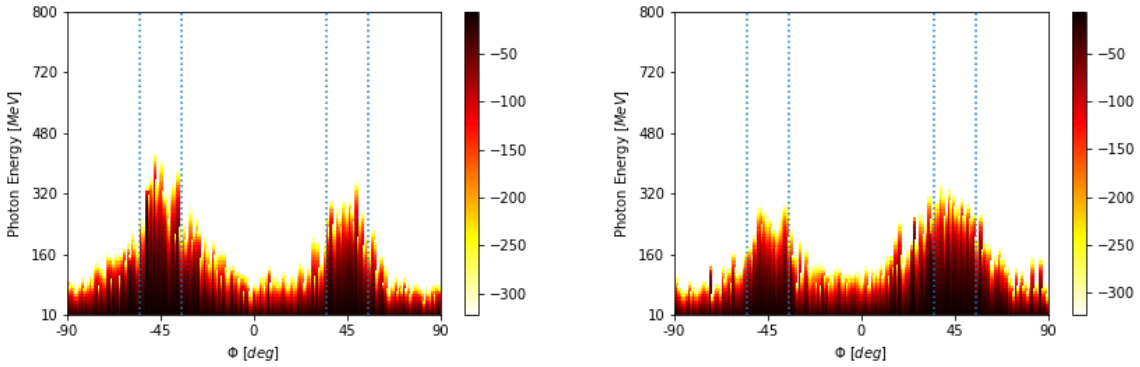

(e) $P_L = 30\,\mathrm{PW}$ (f) $P_L = 40\,\mathrm{PW}$

Figure 25: Angular distribution of photon energy spectrum in *degree* in respect to the channel' symmetric axis and MeV for $a_0 = 350$ at incident powers $P_L = 1$, 5, 10, 20, 30 and 40PW ((a) to (f)) compared as an average of total simulation time. The colorbar gives the number density in units of $log(n_{cr})$ and the dotted blue line indicates the beams defined as the emission cone at $\Phi = \pm 45^{\circ} \pm 10^{\circ}$.

First we take a look at the maximum energies emitted into these beams. The power spectra shown in Fig. 21 depict the maximum photon energies achieved in each simulation pretty accurate, such that the maximum photon energy sampled in Fig. 21 corresponds to the maximum photon energy of the peaks defined as beams. Interestingly the beams aren't symmetrical as one would might assume, additionally this asymmetry does not seem to be strictly one sided. With increasing incident power P_L we observe

rising maximum photon energies as already indicated by the spectra in Fig. 21 as well as a broadening of the emission peaks around $\Phi = \pm 45^{\circ}$. However especially for $a_0 = 350$ this broadening seems to affect the lower energy emissions $\lesssim 200\,\mathrm{MeV}$ more then the higher energy photon emissions up to the most efficient/brilliant beam (see Fig. 26). This is especially visible when comparing Fig. 25 (d) to (e), where the wide lower energy "foundation" around the peak is essentially the same for both incident powers but for $P_L = 30\,\mathrm{PW}$ (e) the amount of high energy photons within the beam is substantially higher than for $P_L = 20\,\mathrm{PW}$ (d) but drops again slightly for $P_L = 40\,\mathrm{PW}$ (f). For $a_0 = 190$ we can see a similar behaviour with the broadening affecting lower energy emission stronger for incident powers up to $P_L = 10\,\mathrm{PW}$. To calculate the conversion efficiency of the lasers energy E_{Laser} into these beams, the total energy radiated by photons with a energy greater than 10 MeV into the left cone at $\Phi = -45^{\circ} \pm 10^{\circ}$ was calculated and depicted for all simulations in Fig. 26 (a) as percentages of E_{Laser}. The first and most obvious is that compared to Fig. 22 and discussed in Section 4.5 we can observe a drop in conversion efficiency into the beam ϵ_{beam} after a peak for both normalized laser amplitudes a_0. For $a_0 = 190$ this drop in conversion efficiency ϵ_{beam} occurs for $P_L \geq 20\,\mathrm{PW}$ with it's maximum at $\epsilon_{beam} \approx 0.03\%$. Additionally we can see that for $P_L = 5\,\mathrm{PW}$ the conversion efficiency peaks above $\epsilon_{beam} \sim 10^{-3}\%$, which is several orders of magnitudes more efficient than for $P_L = 10\,\mathrm{PW}$. For $a_0 = 350$ we see the maximum in conversion efficiency ϵ_{beam} at $P_L = 30\,\mathrm{PW}$, with a maximum conversion efficiency of $\epsilon_{beam} \approx 2.3\%$ Therefor at an incident power P_L above the global conversion efficiency depicted in Fig. 22 (b) at 20 PW. For both normalized amplitudes we see a drastic increase in conversion efficiency going from 1 to 5 PW. Comparing the results for $P_L = 1$ and 20 PW at $a_0 = 190$ with the results found in [26], we find that in general the efficiency observed are some two to three orders of magnitude lower around 4 to 10 PW. For example at $P_L = 10\,\mathrm{PW}$ we measure a conversion efficiency of $\epsilon \sim 0.01‰$ instead of $\sim 1\%$ that was measured in [26]. Although the here measured conversion is not as efficient we can see the same evolution of the efficiency with rising incident power P_L by the spike visible at $P_L = 5\,\mathrm{PW}$ which corresponds the results from [26]. This spike is not visible for $a_0 = 350$. For lower incident powers the conversion efficiency drops to virtually 0 ($\epsilon_{beam} \ll 10^{-20}\%$) for both normalized amplitudes opposing the $\sim 0.2\%$ measured in the aforementioned paper. However, the results in [26] are for a $\tau = 35\,\mathrm{fs}$ laser pulse with normalized amplitude of $a_0 = 190$ at a wavelength of $\lambda = 1\,\mu\mathrm{m}$ hitting a carbon-ion plasma. The shorter pulse duration implies a slightly lower energy input into the plasma by the pulse than for the here used $\tau = 40\,\mathrm{fs}$ laser pulse. More importantly the carbon-ions will likely positively affect the conversion efficiency due to their higher atomic number Z. Globally speaking after the initial rise from 1 to 5 PW we can see the efficiency flattening around the $\epsilon \sim 10^{-3}\%$ mark and slowly reaching it's maximum and then dropping again slowly. Qualitatively this progression is already evident in the angular emission spectra shown in Fig. 24 and Fig. 25. For all incident powers P_L simulated besides 5 and 20 PW the efficiency is higher at the higher normalized laser amplitude $a_0 = 350$. Conclusively the brilliance of the resulting high-energy multi-MeV beam is calculated. For this the number of photons that were emitted into the before defined 20° wide beam around $\Phi = -45^{\circ}$ during the whole simulation time T_{sim} were counted. The divergence

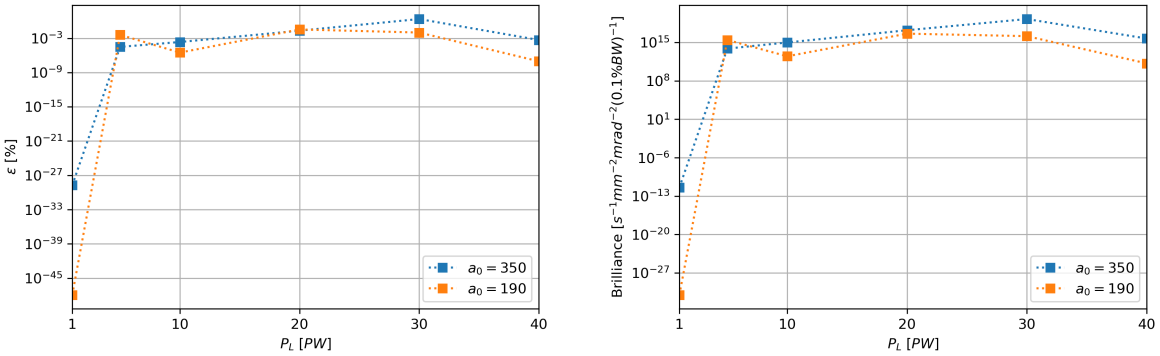

(a) ϵ_{beam}

(b) Corresponding brilliance of beam

Figure 26: Conversion efficiency of laser energy into a high energy γ-ray beam ($\geq 10\,\mathrm{MeV}$) at $\Phi = 45^{\circ} \pm 10^{\circ}$ in percentages of the maximum total energy $U_{tot,max}$ of the system and the corresponding brilliance of those beams in $[\mathrm{s}^{-1}\mathrm{mm}^{-2}\mathrm{mrad}^{-2}(0.1\%BW)^{-1}]$, with the bandwidth referring to the maximum photon energy reached in the individual beam.

was approximated to be equal to the solid angle Ω of the cone extending around the $\Phi = 45^{\circ}$ direction with an opening angle $\Theta = 10^{\circ}$, such that $\Omega = 4\pi \sin^2(\Theta/2)$. The cross sectional area was chosen to be the circular area this cone crosses at a distance of $60\,\mu\mathrm{m}$, which is $1/2$ of the simulation window length in the y-direction. The number of photons falling into $0.1\%BW$ (bandwidth) was calculated by taking the individually highest photon energy reached per simulation as bandwidth and then counting the number of photons within the corresponding highest energy bin that sampled photons. Since the energy bins for sampling had a size of $\sim 8\,\mathrm{MeV}$ each, the percentage of the bandwidth was in all cases above 0.1%, such that the number of photons in the bin had to be individually normalized to achieve this percentage, assuming a linear distribution of photons within these bins. This means that the brilliance values refer to the maximum photon energy in the beam. The brilliance in units of $\mathrm{s}^{-1}\mathrm{mm}^{-2}\mathrm{mrad}^{-2}(0.1\%BW)^{-1}$ for the resulting beams was plotted in Section 4.6 (b). Generally we see a very similar picture as for the conversion efficiency ϵ_{beam}. The before observed patterns translate consistently into the brilliance, besides the beam at $P_L = 20\,\mathrm{PW}$ showing a higher brilliance at $a_0 = 350$ than at $a_0 = 190$, contrary to the conversion efficiency ϵ_{beam} for the same incident power P_L. The maximum brilliance for $a_0 = 190$ is achieved at $P_L = 20\,\mathrm{PW}$ at $4 \times 10^{16}\mathrm{s}^{-1}\mathrm{mm}^{-2}\mathrm{mrad}^{-2}(0.1\%BW)^{-1}$ (at $\sim 92\,\mathrm{MeV}$) and for $a_0 = 350$ at $P_L = 30\,\mathrm{PW}$ at approximately $1.9 \times 10^{19}\mathrm{s}^{-1}\mathrm{mm}^{-2}\mathrm{mrad}^{-2}(0.1\%BW)^{-1}$ (at $\sim 171\,\mathrm{MeV}$. Comparing these brilliance levels to , we find that again our results are two orders of magnitude lower. However the laser pulsed used for these results had a normalized amplitude of $a_0 \approx 468$ with a pulse length of $\tau = 15\,\mathrm{fs}$ [6]. Additionally these results are for another structured plasma target consisting of a $\sim 4n_{cr}$, $22\,\mu\mathrm{m}$ thick hydrogen plasma in front a thin pre-ionized gold layer (Au^{51+}), specifically designed to maximize brilliance [6]. Recognizing these differences within the simulation setup, especially the increase in laser intensity due to the increased normalized amplitude a_0 shows the significance of the presented results as an increase of a_0 in an order of approximately 100 results in an increase of brilliance by about three orders of magnitude. This would suggest that with a similar high normalized amplitude a_0 we would

achieve similar levels of brilliance up to $\sim 10^{22}\mathrm{s}^{-1}\mathrm{mm}^{-2}\mathrm{mrad}^{-2}(0.1\%BW)^{-1}$.

5 Discussion and conclusion

The obvious difference in the trends between global energy conversion efficiency ϵ and conversion efficiency into a collimated and directed high energy beam ϵ_{beam} as defined in Section 4.6 require a careful discussion. As was shown in Fig. 22 and later on visible in the power spectra (Fig. 21), the total radiation energy increases with $a_0 = 190$ strictly for the incident powers simulated up to maximum photon energies of about 180 MeV. For a laser pulse of normalized amplitude of $a_0 = 350$ however total radiation energy seems to saturate for $P_L \gtrsim 30\,\mathrm{PW}$ with a maximum photon energies of about 320 MeV. Due to the increase in energy input with increasing incident power P_L this results in a drop of total energy conversion ϵ for $a_0 = 350$ but not for $a_0 = 190$. It should be clarified ahead that although a second simulation for $a_0 = 190$ at $P_L = 40\,\mathrm{PW}$ was carried out with an extended simulation window to account for the width of the channel required due to the greater focal plane needed for this incident power P_L (see Eq. (3.50)), the results were essentially identical regarding global energy conversion efficiency ϵ. Under the assumption of these two simulations being virtually identical they will be treated as the same simulation. Additionally as visible in Fig. 20 the photon generation relative to incident power P_L, given as the normalized photon number $\tilde{N}_\gamma$ reaches a maximum at $P_L = 10\,\mathrm{PW}$ for both normalized amplitudes. Looking at the generated high-energy multi-MeV beams however tells a different story. As was shown and discussed for Section 4.6 (a) the energy conversion efficiency into the defined beams ϵ_{beam} drops for both normalized amplitudes after reaching a maximum conversion efficiency of $\epsilon_{beam,190} \approx 0.03\%$ and $\epsilon_{beam,350} \approx 2.2\%$ for each respective normalized amplitude. The same behaviour is observed for the brilliance of the beam (Section 4.6 (b)) where for both normalized amplitudes brilliance reaches a maximum and than slowly drops again. The maximum brilliance achieved for $a_0 = 190$ is for $P_L = 20\,\mathrm{PW}$ at $4 \times 10^{16}\mathrm{s}^{-1}\mathrm{mm}^{-2}\mathrm{mrad}^{-2}(0.1\%BW)^{-1}$ (at $\sim 92\,\mathrm{MeV}$) and for $a_0 = 350$ with $P_L = 30\,\mathrm{PW}$ at approximately $1.9 \times 10^{19}\mathrm{s}^{-1}\mathrm{mm}^{-2}\mathrm{mrad}^{-2}(0.1\%BW)^{-1}$ (at $\sim 171\,\mathrm{MeV}$). These results show the same pattern as similar simulations done for recent research [10, 26] although they turn out at smaller values. This is most probably due to the different targets used for these simulations, e.g. carbon-ion plasma instead of H^+-ion plasma, indicating a scaling with atomic number Z of the plasma's ions. To confirm this additional simulations with different plasma compositions are required. Adding the raising presence of filamentation with increasing incident power P_L as a result of increasing plasma channel size as qualitatively discussed in Section 4.3, seems to confirm that as suggested by aforementioned research [13], filamentation instability hinders high-energy photon production. To further quantify the impact of filamentation instability on the generation of high brilliance multi-MeV γ-beams it would be of interest to see the behaviour of these quantities for other ranges of normalized amplitudes. Particularly $a_0 < 190$, still satisfying all conditions of the mildly relativistic regime, probing if increasing occurrence of filamentation further decreases the high-energy photon production as well as $a_0 > 350$ to see if the impact due

to filamentation weakens as the laser spot size and channel width become significantly smaller relative to the growing size of the filaments $q_{\perp}^{-1}$. Changes in the density ratio n_{ch}/n_B might also impact emissions and would offer options for improvement. Further a conical plasma channel that appears to create a single collimated beam instead of two could further improve brilliance of and energy conversion into a γ-photon beam [22]. Additionally a shorter laser pulse duration of $\tau = 10\,\text{fs}$ would make these results more applicable to pending laser facilities like *ELI* and *Apollon*. As PIC-simulations are resource and time demanding the limitations of this thesis made it impossible to investigate all possible parameters to strive for this optimization.

P_L [PW]	1	5	10	20	30	40
$B_{z,max}$ $[B_0]$	0.71	0.87	0.87	1.07	1.06	1.28
$E_{y,max}$ $[E_0]$	0.59	0.86	.096	1.07	1.10	1.25
$\tilde{N}_{\gamma,max}$ $[\times 10^5]$	2.36	15.75	17.99	14.93	12.98	10.33
$\varepsilon_{\gamma,max}$ [MeV]	36	112	104	96	92	96
ϵ [%]	1.38	2.87	3.29	3.97	4.44	4.59
ϵ_{beam} [%]	1.13×10^{-48}	4.02×10^{-3}	3.15×10^{-6}	3.52×10^{-2}	1.01×10^{-2}	9.38×10^{-8}
Brill.	9.38×10^{-32}	2.86×10^{15}	3.01×10^{12}	4.01×10^{16}	1.40×10^{16}	1.52×10^{11}

(a) $a_0 = 190$

P_L [PW]	1	5	10	20	30	40
$B_{z,max}$ $[B_0]$	0.34	0.84	0.82	0.86	0.98	0.96
$E_{y,max}$ $[E_0]$	0.27	0.76	0.84	0.89	0.89	0.88
$\tilde{N}_{\gamma,max}a$ $[\times 10^5]$	1.48	9.61	13.47	10.98	7.78	6.68
$\varepsilon_{\gamma,max}$ [MeV]	36	116	136	172	223	152
ϵ [%]	1.07	2.76	2.85	2.29	1.96	1.83
ϵ_{beam} [%]	1.82×10^{-29}	3.14×10^{-5}	2.24×10^{-4}	2.15×10^{-2}	2.36	5.03×10^{-4}
Brill.	3.60×10^{-12}	7.59×10^{13}	9.88×10^{14}	1.68×10^{17}	1.86×10^{19}	5.15×10^{15}

(b) $a_0 = 350$

Table 3: Table of characteristic simulation results rounded to second digit, except maximum photon energy $\varepsilon_{\gamma,max}$. Maximum values depict the overall maximum of that value during the whole simulation. Brilliance (Brill.) is in units of $\text{s}^{-1}\text{mm}^{-2}\text{mrad}^{-2}(0.1\%BW)^{-1}$ with the chosen bandwidth energy corresponding to $\varepsilon_{\gamma,max}$.

References

[1] Akhmanov, S A. ; Sukhorukov, Anatolii P. ; Khokhlov, R V.: SELF-FOCUSING AND DIFFRACTION OF LIGHT IN A NONLINEAR MEDIUM. In: *Soviet Physics Uspekhi* 10 (1968), Nr. 5, S. 609–636. – ISSN 0038–5670 and 2169–5296

[2] Aléonard, M. ; Altarelli, M. ; Antici, Patrizio ; Apolonskiy, Alexander ; Audebert, Patrick ; Bartnik, Andrzej ; Barty, C. ; Bernstein, A. ; Biegert, Jens ; Böni, P. ; Booth, Nicola ; Bote, D. ; Bulanov, S. ; Butkus, Rytis ; Cardoso, Luis ; Chambaret, J.P. ; Charambilidis, D. ; Cheriaux, G. ; Clarke, R. ; Zepf, M.: *WHITEBOOK ELI – Extreme Light Infrastructure; Science and Technology with Ultra-Intense Lasers*. 2011. http://dx.doi.org/10.13140/2.1.1227.0889. http://dx.doi.org/10.13140/2.1.1227.0889

[3] Cowan, Benjamin M. ; Bruhwiler, David L. ; Cormier-Michel, Estelle ; Esarey, Eric ; Geddes, Cameron G. ; Messmer, Peter ; Paul, Kevin M.: Characteristics of an envelope model for laser–plasma accelerator simulation. In: *Journal of Computational Physics* 230 (2011), Nr. 1, S. 61–86. – ISSN 0021–9991 and 1090–2716

[4] Derouillat, J ; Beck, A ; Pérez, F ; Vinci, T ; Chiaramello, M ; Grassi, A ; Flé, M ; Bouchard, G ; Plotnikov, I ; Aunai, N ; Dargent, J ; Riconda, C ; Grech, M: Smilei : A collaborative, open-source, multi-purpose particle-in-cell code for plasma simulation. In: *Computer Physics Communications* 222 (2018), S. 351–373. – ISSN 0010–4655 and 1879–2944

[5] Di Piazza, A. ; Müller, C. ; Hatsagortsyan, K. Z. ; Keitel, C. H.: Extremely high-intensity laser interactions with fundamental quantum systems. In: *Rev. Mod. Phys.* 84 (2012), Aug, 1177–1228. http://dx.doi.org/10.1103/RevModPhys.84.1177. – DOI 10.1103/RevModPhys.84.1177

[6] Gu, Yan-Jun ; Klimo, Ondrej ; Bulanov, Sergei V. ; Weber, Stefan: Brilliant gamma-ray beam and electron–positron pair production by enhanced attosecond pulses. In: *Communications Physics* 1 (2018), Nr. 1, S. 1–9. – ISSN 2399–3650 and 2399–3650

[7] Ivanov, D. ; Kotkin, G. ; Serbo, V.: Complete description of non-linear compton and BREIT-wheeler processes. In: *Acta Physica Polonica B* 37 (2006), 04

[8] Jackson, John D.: *Klassische Elektrodynamik*. 5., überarbeitete Auflage. Berlin ; Boston : de Gruyter, 2014 (De Gruyter Studium). – Online–Ressource (XIX, 938 S.). http://dx.doi.org/10.1515/9783110334470. http://dx.doi.org/10.1515/9783110334470. – ISBN 978–3–11–033447–0

[9] Jansen, O ; Wang, T ; Stark, D J. ; d'Humières, E ; Toncian, T ; Arefiev, A V.: Leveraging extreme laser-driven magnetic fields for gamma-ray generation and pair production. In: *Plasma Physics and Controlled Fusion* 60 (2018), mar, Nr. 5, 054006. http://dx.doi.org/10.1088/1361-6587/aab222. – DOI 10.1088/1361–6587/aab222

[10] Jansen, Oliver ; Wang, T. ; Gong, Zheng ; Ribeyre, Xavier ; Humì, E ; Stutman, D ; Toncian, Toma ; Arefiev, Alex: Collimated gamma-ray beams from structured laser-irradiated targets - how to increase the efficiency without increasing the laser intensity. (2019), 08

[11] Jung, Ralph: *Laser-plasma interaction with ultra-short laser pulses*. VDM-Verlag Dr. Müller, 2008

[12] Kaw, P. ; Schmidt, G. ; Wilcox, T.: Filamentation and trapping of electromagnetic radiation in plasmas. In: *The Physics of Fluids* 16 (1973), Nr. 9, 1522-1525. http://dx.doi.org/10.1063/1.1694552. – DOI 10.1063/1.1694552

[13] Kumar, Naveen ; Tripathi, V K. ; Sawhney, B K.: Filamentation of a relativistic short pulse laser in a plasma. In: *Physica Scripta* 73 (2006), Nr. 6, S. 659–662. – ISSN 1402–4896 and 0031–8949 and 1402–4896

[14] Marklund, Mattias ; Shukla, Padma K.: Nonlinear collective effects in photon-photon and photon-plasma interactions. In: *Rev. Mod. Phys.* 78 (2006), May, 591–640. http://dx.doi.org/10.1103/RevModPhys.78.591. – DOI 10.1103/RevModPhys.78.591

[15] Mourou, Gerard A. ; Tajima, Toshiki ; Bulanov, Sergei V.: Optics in the relativistic regime. In: *Reviews of Modern Physics* 78 (2006), Nr. 2, S. 309–371. – ISSN 0034–6861 and 1539–0756

[16] Nakamura, Tatsufumi ; Koga, James K. ; Esirkepov, Timur Z. ; Kando, Masaki ; Korn, Georg ; Bulanov, Sergei V.: High-power -ray flash generation in ultraintense laser-plasma interactions. In: *Physical review letters* 108 (2012), Nr. 19, S. 195001. – ISSN 0031–9007 and 1079–7114

[17] Papadopoulos, D.N. ; Zou, J.P. ; Le Blanc, C. ; Chériaux, G. ; Georges, P. ; Druon, F. ; Mennerat, G. ; Ramirez, P. ; Martin, L. ; Fréneaux, A. ; al. et: The Apollon 10 PW laser: experimental and theoretical investigation of the temporal characteristics. In: *High Power Laser Science and Engineering* 4 (2016), S. e34. http://dx.doi.org/10.1017/hpl.2016.34. – DOI 10.1017/hpl.2016.34

[18] Povh, Bogdan ; Rith, Klaus ; Scholz, Christoph ; Zetsche, Frank ; Rodejohann, Werner: *Teilchen und Kerne*. 9. Aufl. 2014. Berlin, Heidelberg : Springer Spektrum, 2014 (SpringerLink : Bücher). – Online–Ressource (XII, 467 S. 160 Abb, online resource). http://dx.doi.org/10.1007/978-3-642-37822-5. http://dx.doi.org/10.1007/978-3-642-37822-5. – ISBN 978–364–23782–2–5

[19] Sakai, Y ; Williams, O ; Andonian, G ; Fukasawa, A ; Hemsing, E ; Marinelli, A ; Barber, S ; O'Shea, FH ; Rosenzweig, JB: Harmonic radiation of a relativistic nonlinear inverse Compton scattering using two laser wavelengths. In: *Physical Review Special Topics-Accelerators and Beams* 14 (2011), Nr. 12, S. 120702

[20] Sharma, S ; Kumar, N ; Hussain, S ; Sharma, R.P: Nonlinear evolution of the filamentation instability and chaos in laser–plasma interaction. In: *Laser and Particle Beams* 35 (2017), Nr. 1, S. 10–18. – ISSN 0263–0346 and 1469–803X

[21] Sheng, Z. M. ; Nishihara, K. ; Honda, T. ; Sentoku, Y. ; Mima, K. ; Bulanov, S. V.: Anisotropic filamentation instability of intense laser beams in plasmas near the critical density. In: *Phys. Rev. E* 64 (2001), Nov, 066409. http://dx.doi.org/10.1103/PhysRevE.64.066409. – DOI 10.1103/PhysRevE.64.066409

[22] Stark, David ; Toncian, Toma ; Arefiev, Alex: Enhanced Multi-MeV Photon Emission by a Laser-Driven Electron Beam in a Self-Generated Magnetic Field. In: *Physical Review Letters* 116 (2016), 05. http://dx.doi.org/10.1103/PhysRevLett.116.185003. – DOI 10.1103/PhysRevLett.116.185003

[23] Sun, Guo-Zheng ; Ott, Edward ; Lee, Y. C. ; Guzdar, Parvez: Self-focusing of short intense pulses in plasmas. In: *The Physics of Fluids* 30 (1987), Nr. 2, 526-532. http://dx.doi.org/10.1063/1.866349. – DOI 10.1063/1.866349

[24] Umstadter, Donald: Relativistic laser–plasma interactions. In: *Journal of Physics D: Applied Physics* 36 (2003), Nr. 8, S. R151–R165. – ISSN 0022–3727 and 1361–6463

[25] v2, Piachoo: *Grin-lens.png*. https://upload.wikimedia.org/wikipedia/commons/2/2c/Grin-lens.png. Version: 20th April 2020

[26] Wang, T. ; Ribeyre, X. ; Gong, Z. ; Jansen, O. ; d'Humières, E. ; Stutman, D. ; Toncian, T. ; Arefiev, A.: Power Scaling for Collimated γ-Ray Beams Generated by Structured Laser-Irradiated Targets and Its Application to Two-Photon Pair Production. In: *Phys. Rev. Applied* 13 (2020), May, 054024. http://dx.doi.org/10.1103/PhysRevApplied.13.054024. – DOI 10.1103/PhysRevApplied.13.054024

[27] Wu, Yuan-Bin ; Xue, She-Sheng: Nonlinear Breit-Wheeler process in the collision of a photon with two plane waves. In: *Physical Review D* 90 (2014), Jul, Nr. 1. http://dx.doi.org/10.1103/physrevd.90.013009. – DOI 10.1103/physrevd.90.013009. – ISSN 1550–2368

[28] Xue, Kun ; Dou, Zhen-Ke ; Feng, Wan ; Tong-Pu, Yu ; Wang, Wei-Min ; Ren, Jie-Ru ; Zhao, Qian ; Zhao, Yong-Tao ; Xu, Zhong-Feng ; Li, Jian-Xing: Generation of highly-polarized high-energy brilliant γ-rays via laser-plasma interaction. (2020), 03

Erklärung der Eigenständigen Anfterigung

Ich versichere, dass ich diese Arbeit selbstständig verfasst und keine anderen als die angegebenen Quellen und Hilfsmittel benutzt habe.

Heidelberg, den 23. Juni 2020,